Non-equilibrium Quantum Transport in Two Dimensional Electron Gases in Modulation Doped Heterostructures

A DISSERTATION
SUBMITTED TO THE FACULTY OF THE
UNIVERSITY OF MINNESOTA
BY

Quentin Alexander Ebner

IN PARTIAL FULFILLMENT OF THE REQUIREMENTS
FOR THE DEGREE OF
DOCTOR OF PHILOSOPHY

ADVISOR: Michael Zudov

August, 2017

Acknowledgments

I would like to thank my professor, Michael Zudov, and fellow graduate student, Qianhui Shi, for discussions about my research throughout my time as a graduate student.

Abstract

This thesis focuses on experimental investigations of transport in two dimensional electron gases (2DEG) driven out of equilibrium by microwaves and dc current. Part I presents the background information and is broken into four sections. The first section discusses the basics of transport and measurements in a 2DEG, highlighting the origins of disorder in the formation of modern heterostructures and the fundamental properties of a 2DEG. The second through fourth sections discuss magneto transport in 2DEGs with the second part discussing Shubnikov-de Haas Oscillations. The third section looks into the experimental and theoretical background of microwave-induced resistance oscillations (MIRO), which arise in the magnetoresistance of a 2DEG under microwave irradiation. The fourth section presents Hall field-induced resistance oscillations (HIRO), which arise in the magnetoresistance of a 2DEG with an applied dc current.

The second part of this thesis is broken into three sections that each discuss experimental findings of MIRO and HIRO in various 2DEGs. The fifth section discusses the observation of MIRO and HIRO in p-type Germanium quantum wells. This is significant because previous studies into a variety of different materials never showed any MIRO response. P-type Germanium is the second material for which MIRO and HIRO have been observed, making MIRO and HIRO not unique to GaAs quantum wells.

The sixth section looks into the role of introducing alloy disorder into the quantum well on MIRO and HIRO. The quantum scattering rate was found to increase with the amount of alloy disorder and the MIRO prefactor that is decided by scattering times was not found to have a measurable change with increasing alloy disorder concentration. It was found the amplitude of HIRO is controlled by sharp disorder scattering contribution in mobility.

The seventh section provides a systematic study into the effects of density on MIRO, which is not well understood. The analysis focuses on when one energy sub-band is populated, but also gives some observations of when two sub-bands are

populated. When one sub-band is populated, increasing density was found to suppress the effective mass extracted from MIRO. The change in MIRO amplitude was found to be described by a combination of the zero-field resistance and the increase of quantum lifetime as density increased. When the second sub-band was populated, MIRO was found to be highly suppressed and this suppression cannot be explained by the MIRO mechanisms, quantum lifetime, or MIRO's power factor.

Table of Contents

List of Tables

List of Figures

Part I

Background Information

I. TWO-DIMENSIONAL ELECTRON GAS

One of the most important tools in low dimensional physics is the two-dimensional electron gas (2DEG). These 2DEGs are made from semiconductor materials, with the AlGaAs/GaAs heterostructures being the most prominently studied. Modern techniques, such as molecular beam epitaxy (MBE), have allowed the quantum wells to be formed with very little disorder and provided a good method for controlling the amount and type of disorder present (Manfra, 2014). This chapter will present how a quantum well is formed and discuss the types of disorder that can be present in 2DEGs and how modern heterostructures have been further improved.

A. Forming a Quantum Well

The modern heterostructures studied in this thesis use modulation doping, and will be described in terms of an AlGaAs/GaAs heterostructure. Adding donors directly to the quantum well will leave undesirable charged impurities in the transport channel. To avoid this, a doped region with charge carriers is grown near an undoped region and the charge carriers will migrate over to the undoped region. This is known as modulation doping. To understand why the charge carriers will migrate, consider n-type AlGaAs (doping layer) next to undoped GaAs (quantum well). Fig. 1 shows the band structure of the GaAs/AlGaAs interface before taking internal electronic processes into account. Here, the Fermi energy for AlGaAs is just below the energy of the conduction band and the Fermi energy for GaAs is just above the valence band. The AlGaAs has intentionally been doped n-type so that the conduction band has mobile electrons. A few of the valence electrons will move to fill the holes in the top of the GaAs valence band, while most of the remaining electrons will end up in the bottom of the GaAs conduction band. We are then left with a positive charge on the donor impurities which attracts the electrons in the GaAs conduction band to the interface, thus bending the bands in the process. This attraction that bends the band structure generates an internal electric field. The process of electrons moving from AlGaAs to GaAs continues until a strong enough dipole layer forms, which makes the Fermi level of the GaAs equal to the Fermi level of the AlGaAs as seen in Fig. 2.

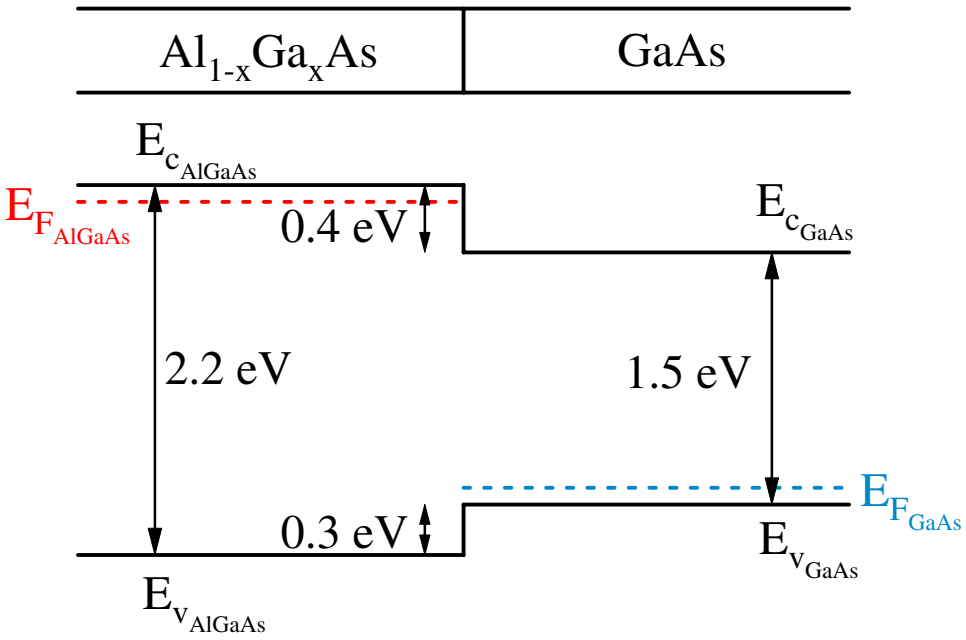

FIG. 1 [Adapted from (Hatke, 2011)] Band structure for GaAs/AlGaAs heterostructure before taking electronic processes into account. The doping layer is the $Al_{1-x}Ga_xAs$ and the quantum well is the GaAs. The Fermi energy level is just below the bottom of the conduction band for AlGaAs and just above the valance band for GaAs.

This causes the density of electrons in GaAs/AlGaAs heterostructures to be fixed and dependent on the dopant density.

Further refinement of modulation doping comes in the form of adding a neutral undoped AlGaAs layer called a spacer between the doping layer and the quantum well. Thus, this structure is primarily characterized by 3 consecutive layers: n-type AlGaAs doped with Si, neutral AlGaAs, and undoped GaAs. The spacer can be anywhere from a few nanometers to hundreds of nanometers and is used to control both the density of free charge carriers that migrate to the quantum well and how much the charged scattering centers from the doping can affect the electrons in the quantum well. If one still wants control of the density, one can add a back gate; however, this is not necessary for the formation of the 2DEG.

Apart from $GaAs/Al_xGa_{1-x}As$ heterostructures, this thesis will also look at p-type Ge/SiGe heterostructures, where holes move instead of electrons. Their structure is similar to the $GaAs/Al_xGa_{1-x}As$ heterostructures with the three main layers being

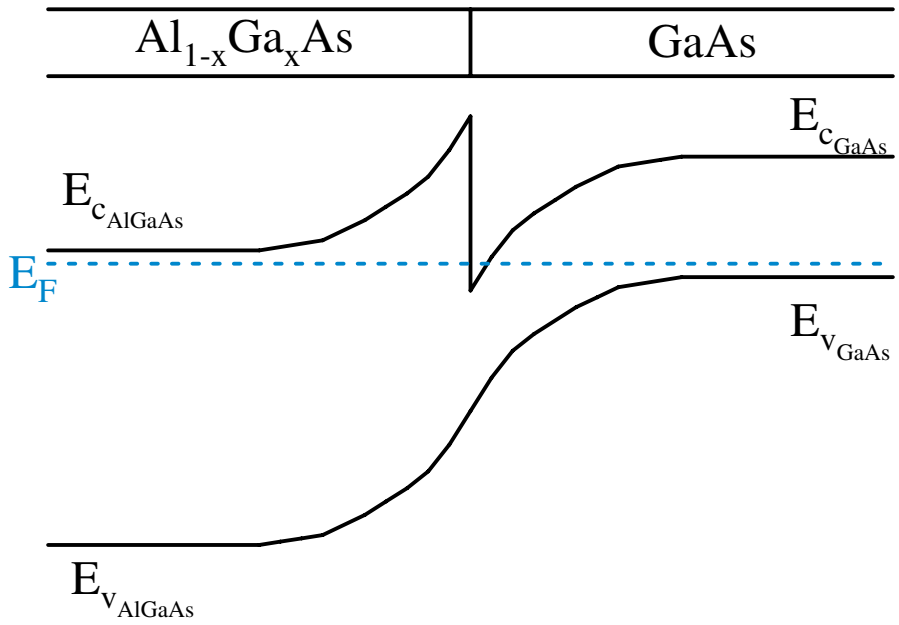

FIG. 2 [Adapted from (Hatke, 2011)] Band structure after electronic processes are accounted for. The Fermi energy levels of AlGaAs and GaAs are forced to line up. The first conduction sub-band of the potential well in the GaAs is populated by donor electrons from $Al_xGa_{1-x}As$ that tunnel through the potential barrier. Not shown is an undoped AlGaAs layer which separates the donors from the interface.

a SiGe donor layer doped with Boron, a neutral SiGe spacer, and a Ge quantum well. The Ge/SiGe samples used are created through reduced pressure chemical vapor deposition (RPCVD) instead of MBE, which results in layers that are less anatomically sharp than those done by MBE, but still are considered anatomically sharp. The resulting strained Ge quantum well will still be 99.99% pure Ge.

1. Modern Heterostructures

The previously described heterostructure consisting of a donor layer, spacer, and quantum well is a good structure; however, there are a couple limitations that it has which have lead to improvements in heterostructure design. The first improvement is to create a symmetric quantum well by having a spacer and donor layer on both sides of the quantum well. This allows for larger densities to be achieved since there

are now two channels providing charge carriers to the quantum well. Furthermore, the symmetric design pushes the charge carriers to the center of the quantum well, reducing interface roughness scattering (Manfra, 2014).

Another improvement is to the structure of the donor layers. By doping a layer of AlGaAs with Si, the donor atom can distort the AlGaAs crystal to form what is known as a DX center (Davies, 1998). This distortion of the lattice leads to an increase in the binding energy of the donors, which creates an energy barrier that needs to be overcome in order to trap electrons. Below about 150 K, the thermal energy is insufficient to allow electrons to become trapped in the DX centers. This means that by illuminating the sample at low temperatures (for example with an LED), the electrons are released from the DX centers and can permanently contribute to conduction, leading to increased density. Thus, in order to put a sample in its best condition, it must be illuminated at low temperatures.

To improve on this, the single AlGaAs doped donor layer is replaced with 3 layers: a Si doped GaAs layer surrounded by a neutral AlAs layer on each side. These layers are normally about 2-3 nm thick. When charge carriers then migrate to the quantum well, some remain in the AlAs layers and for certain doping levels, no significant parallel conduction will occur (Manfra, 2014). These electrons in the AlAs then screen the potential of the parent ions. Also, since the Si doping is in GaAs instead of AlGaAs, no DX centers are formed meaning illumination is not needed to achieve maximum density. However, illumination at low temperatures is still often used since it still often improves the quality of phenomena studied in these systems. It is not well understood why illumination improves this heterostructure design, but it is believed that it causes a redistribution of charge to better screen the fluctuations caused by the disorder potential (Manfra, 2014).

2. Molecular Beam Epitaxy

The importance 2DEG's has been largely brought about by the modern growth technique known as molecular beam epitaxy (MBE), which is used to create ultra-clean, high-mobility ($\mu > 10^7$ cm^2/Vs) AlGaAs/GaAs. One of the most notable

features of MBE is the extremely slow and uniform growth of the heterostructures, which allows for very precise thickness of layers to be able to be formed and very abrupt interfaces between layers of different materials (Manfra, 2014). A typical growth speed is 0.1 to 2 mono-layers per second, which provides an acceptable amount of reproducibility.

MBE involves placing the substrate upon which the sample is to be grown on a holder in an ultra high vacuum environment, typically 10^{-12} torr, which helps prevent unintentional charged impurities from being introduced through any residual gases present during the growth. The materials used to create the heterostructure are placed in furnaces with a shuttered opening pointing toward the substrate. These furnaces, called Knudsen cells or K-cells, are then set to high enough temperatures to vaporize the materials. The shutters are then opened and closed at various intervals to allow the vaporized materials to form molecular beams that are deposited on the substrate. A beam is formed because diffusion as seen at higher pressures is not seen in such systems due to the extremely low pressures. In fact, the pressures are low enough that the mean-free path of the molecules is much longer than the size of the growth chamber.

While the basic operations are simple to understand actually implementing the growth process to create high quality samples is not so simple. Here are a few considerations of the growers that show this point (Davies, 1998). The starting materials in the K-cells need to be extremely pure and must not be polluted by the K-cells to prevent contamination. Also, the flux of particles across the substrate needs to be uniform to prevent variations in sample composition. Each material composition that is deposited grows better under different conditions.

B. Disorder and Scattering

Disorder in these high-mobility structures is very important to understand because it strongly influences the scattering interactions that occur in the sample. Here we will look at the two main contributions to the disorder potential in our high-mobility structures.

The first type of disorder present is due to the limitations of growing quantum wells. Even growing the quantum well with MBE, there will still be some dislocations and defects in the surface of the quantum well which lead to short range scattering events (Manfra, 2014). These short range scattering events will cause large angle scattering of electrons in the 2DEG and are also referred to as sharp scattering. Sources of this type of disorder include not having a pure source for growing the structures, interface roughness scattering, and defects in the lattice.

The second type of disorder present is due to using a spacer to keep the remote donors far from the 2DEG. Often one wants as small of spacer as possible to create the largest possible carrier density. However, the remote donors are charged so their electric fields can interact with the charge carriers that travel through the quantum well. These interactions are unwanted so increasing the spacer thickness as much as possible is also desired. By adjusting the thickness of the spacer, one is able to affect how the charge carriers interact with the disorder potential created by the donors. Most often, the spacer is set sufficiently large (70 nm) so that scattering events are primarily small angle scattering events, also called smooth scattering.

These two types of disorder can be combined into a common disorder model, or a mixed disorder model, in which the elastic scattering rate through any angle is expressed by: (Khodas and Vavilov, 2008)

$$\frac{1}{\tau_\theta} = \sum_{n=-\infty}^{\infty} \frac{e^{in\theta}}{\tau_n}, \quad \tau_n = \tau_{-n} \tag{1}$$

The individual harmonics are expressed in terms of the sharp (τ_{sh}) and smooth (τ_{sm}) scattering rates by

$$\frac{1}{\tau_n} = \frac{\delta_{0,n}}{\tau_{\mathrm{sh}}} + \frac{1}{\tau_{\mathrm{sm}}} \frac{1}{1+\chi n^2} \tag{2}$$

where $\chi = (k_F d)^{-2}$ with k_F being the Fermi wave-vector and d the width of the spacer separating the donors and the quantum well. For example, in a later section where we will discuss the transport scattering time τ, we can represent this scattering time in terms of angular harmonics by $\tau^{-1} = \tau_0^{-1} - \tau_1^{-1}$.

C. Drude Theory

The simplest theory describing the electric conductivity of a system is an application of kinetic theory which was proposed by Drude in 1900. Here Drude theory will be covered, treating the electrical properties of conductors in a semi-classical manner. The consequences of quantum mechanics such as the formation of Landau Levels will be treated in Sec I D *1.*

1. Electrical Transport when $B = 0$

Conductivity, σ, and resistivity, ρ, are best understood through the following equations:

$$\boldsymbol{j} = \sigma \boldsymbol{E}, \qquad \boldsymbol{E} = \rho \boldsymbol{j} \tag{3}$$

where $\boldsymbol{j}$ is the current density and $\boldsymbol{E}$ is an applied electric field. From these expressions it is seen that these two properties actually describe the same physical properties in a material. The difference between the expressions is in their measurement set-ups. When measuring conductivity, one applies an electric field and measures a current, while when measuring resistivity, one applies a current and measures a voltage drop.

Drude theory is a semi-classical approach in which it is assumed the motion of electrons can be treated classically which is seen by the fact that electrons elastically scatter off disorder. In this picture, an electron of charge $-e$ and velocity of v goes an average distance of $l_o = v\tau$ over a time τ before being scattered to a new velocity of which the average new velocity is zero. If we then place the electron, of mass m, is in a weak electric field E, it will pick up an average drift velocity of:

$$\boldsymbol{v} = \frac{e\tau}{m}\boldsymbol{E} = \mu \boldsymbol{E} \tag{4}$$

where μ is the electron mobility and τ is commonly referred to as the transport scattering time. Inserting Eq. (4) into the the expression for current density, $\boldsymbol{j} = n_e e \boldsymbol{v}$, one finds:

$$\boldsymbol{j} = \frac{ne^2\tau}{m}\boldsymbol{E} = \sigma_0 \boldsymbol{E} \tag{5}$$

where n is the carrier density, providing an expression for the zero-field Drude conductivity σ_0.

The theory is said to be semi-classical because quantum effects can be added without a change in the overall form of the conductivity. Quantum effects will enter through the band structure, which changes the electron mass to an effective mass $m^\star$ and through the value of τ, giving a final form of:

$$\boldsymbol{j} = \frac{ne^2\tau}{m^\star}\boldsymbol{E} = \sigma_0\boldsymbol{E}, \qquad \boldsymbol{E} = \rho_0\boldsymbol{j} = \frac{m^\star}{ne^2\tau}\boldsymbol{j} \tag{6}$$

2. Electrical Transport when $B \neq 0$

Now a magnetic field is applied to the quantum well, which means the electrons will also be under the effect of the Lorentz force. This is taken into account by modifying the current density, which results in it being of the form $\boldsymbol{j} = \sigma_{\mathrm{D}}(\boldsymbol{E} - \boldsymbol{v} \times \boldsymbol{B})$. Current and electric field will no longer be parallel leading to σ and ρ to both be expressed as tensors:

$$\sigma = \begin{bmatrix} \sigma_{xx} & \sigma_{xy} \\ \sigma_{yx} & \sigma_{yy} \end{bmatrix} \qquad \rho = \begin{bmatrix} \rho_{xx} & \rho_{xy} \\ \rho_{yx} & \rho_{yy} \end{bmatrix} \tag{7}$$

When the applied field is perpendicular to the quantum well, the resistivity now takes the form

$$\rho = \begin{bmatrix} \rho_0 & B/ne \\ -B/ne & \rho_0 \end{bmatrix} = \rho_0 \begin{bmatrix} 1 & \omega_c\tau \\ -\omega_c\tau & 1 \end{bmatrix} \tag{8}$$

where $\omega_c = eB/m^\star$ is the cyclotron frequency. The product $\omega_c\tau$ describes how many cyclotron orbits an electron experiences before it scatters.

Given how conductivity and resistivity are defined, they are the inverse of each other, which allows one to express the conductivity in terms of the resistivity:

$$\sigma_{xx} = \frac{\rho_{xx}}{\rho_{xx}^2 + \rho_{xy}^2}; \quad \sigma_{xy} = \frac{\rho_{xy}}{\rho_{xx}^2 + \rho_{xy}^2}. \tag{9}$$

Under the case where $\rho_{xy} \gg \rho_{xx}$, we find $\sigma_{xx} \propto \rho_{xx}$.

D. Energy Quantization

Drude theory provides good insight into 2DEGs through the conductivity and resistivity; however, one also needs to use quantum mechanics to further understand

at the nature of a 2DEG. Here an oscillating density of states will be developed and discussed since it serves as a basis for all of the phenomena studied in this thesis.

1. Landau Levels

The quantum nature of the 2DEG begins with the Schrödinger equation of a free 2DEG, confined to the x-y plane, in a perpendicular magnetic field, B,

$$E\Psi(\mathbf{r}) = \left[\frac{(\mathbf{p}+e\mathbf{A})^2}{2m^\star} + V(z)\right]\Psi(\mathbf{r}) = H_0\Psi(\mathbf{r}) \tag{10}$$

where $V(z)$ is a confining potential and $(\mathbf{p}+e\mathbf{A})^2/2m^\star$ is the kinetic energy. The z-direction can be completely neglected since the potential is additive and is not affected by the magnetic field. It is convenient to adopt the Landau gauge to solve this equation, which requires assuming the vector potential takes the form $\mathbf{A} = (-By, 0, 0)$ which allows the Hamiltonian to be written as

$$H_0 = \frac{1}{2m^\star}\left[(p_x - eBy)^2 + p_y^2\right]. \tag{11}$$

This resulting Hamiltonian can be separated into its x and y pieces, and it can be further reduced into a 1D equation of the form

$$E\Psi(y) = \frac{\hbar\omega_\mathrm{c}}{2}\left[-l_B^2\frac{\partial^2}{\partial y^2} + \left(\frac{y}{l_B} - l_B k_x\right)^2\right]\Psi(y) \tag{12}$$

where $l_B = \sqrt{\hbar/eB}$ is the magnetic length. This is now in the form of the Schrödinger equation for the quantum harmonic oscillator, where for Ψ there is energy $E = \hbar\omega_\mathrm{c}(N+1/2)$. This result presents the energy spectrum as a series of discrete energy levels with spacing $\hbar\omega_\mathrm{c}$. The energy levels are referred to as Landau Levels (LLs).

2. Fermi Energy

Assuming the 2DEG is at zero temperature, the density of states in K-space is $2/(2\pi)^2$ and the area of the Fermi surface is circular with area πk_F^2 which gives a density:

$$n_e = \frac{k_\mathrm{F}^2}{2\pi} \tag{13}$$

where k_{F} is the Fermi wave vector. The Fermi Energy describes the highest filled energy state in a material and since these are free electrons it is expressed by:

$$E_{\mathrm{F}} = \frac{\hbar^2 k_{\mathrm{F}}^2}{2m^\star} = \frac{\hbar^2 \pi n_e}{m^\star} \tag{14}$$

Thus to adjust the Fermi energy, one adjusts the density.

The energy of the LLs was given to be $E = \hbar\omega_{\mathrm{c}}(N + 1/2) \propto B^{-1}$. Now for a fixed density and depending on the magnetic field, the electrons in the system will be confined to a set of energy levels corresponding to that magnetic field.

3. Oscillating Density of States

The density of states (DOS), $\nu(\varepsilon)$, for a sample with out disorder, at $T = 0$, and in a magnetic field is a series of delta functions at the energies of the LLs, ε_N, given by (Davies, 1998)

$$\nu(\varepsilon) = \frac{1}{2\pi l_B^2} \sum_N \delta(\varepsilon - \varepsilon_N). \tag{15}$$

When one takes into account disorder and temperature, there is a smearing of the Fermi surface or a broadening of the LL. For $N \gg 1$ and using a quasi-classical approximation in the limit of overlapping LLs, $\omega_{\mathrm{c}}\tau_{\mathrm{q}} \ll 1$, the density of states for the Nth Landau Level becomes a series of Gaussians: (Dmitriev et al., 2012)

$$\nu^{(N)}(\varepsilon) = \frac{1}{2\pi l_B^2} \left(\frac{\tau_{\mathrm{q}}}{\omega_{\mathrm{c}}}\right)^{1/2} \exp\left[-\frac{\pi\tau_{\mathrm{q}}}{\omega_{\mathrm{c}}}(\varepsilon - \varepsilon_N)^2\right] \tag{16}$$

where τ_{q} is the quantum lifetime. The quantum scattering rate represents the width the LLs. A series of equally-spaced, overlapping Gaussians gives rise to a total DOS of (Dmitriev et al., 2012)

$$\nu(\varepsilon) = \nu_0 \left[1 + 2\sum_{k=1}^{\infty} (-1)^k \lambda^{k^2} \cos\left(\frac{2\pi k\varepsilon}{\omega_{\mathrm{c}}}\right)\right] \tag{17}$$

where $\nu_0 = m^\star/2\pi\hbar$ is the DOS per spin at $B = 0$ and λ is the Dingle factor and is expressed as

$$\lambda = \exp\left(-\frac{\pi}{\omega_{\mathrm{c}}\tau_{\mathrm{q}}}\right). \tag{18}$$

Eq. (17) now shows that the density of states is oscillatory in B^{-1} since $\omega_{\mathrm{c}} \propto B$.

Unlike the transport lifetime from Drude theory, τ_q is highly affected by small angle scattering. Since the systems studied in this thesis are highly affected by small angle scattering due to modulation doping of the samples, this leads to a significant difference between the two scattering times: $\tau \approx 1$ ns and $\tau_q \approx 10$ ps.

4. Sub-bands

When dealing with the Schrödinger equation previously, the confining potential, $V(z)$, was ignored. When one takes into account the confining potential, one finds that it has its own set of allowed energies dependent on the geometry of the well. Similar to Sec I.D.*2*, depending on the Fermi Energy (i.e. the density), the number of energy levels that are filled changes. The energy levels attached to these energy bands are often referred to as quantum well sub-bands (or just sub-bands for short). Unless otherwise noted, all experiments in this thesis will be dealing with only one occupied sub-band.

E. Measurements

The measurements performed in this thesis will be done on two different types of geometries of 2DEGs, Van der Pauw (VdP) or Hall bar structures. The simpler geometry to create is the VdP, which is a square with either 4 or 8 contacts located on the edges of the sample. When there are 4 contacts, they are in the corners of the sample, if there are 8 contacts, they are located in the corners and in the middle of each side. Hall bars have the benefit of being a better defined geometry and are necessary for experiments that require the width of the sample to be defined; however, they take significantly more effort to fabricate. An example of a Hall bar is shown in Fig. 3.

As stated before, the Hall bar has better defined geometry, what we mean by that is the current path is better defined. A VdP is often 3x3 mm or 4x4 mm and has contacts on the edges, while a Hall bar will often be 2-3 mm long and have a width of less than 200 μm and contacts are connected to the Hall bar by a thin path as seen in Fig. 3. This leads to the paths the current can take being more limited/more well

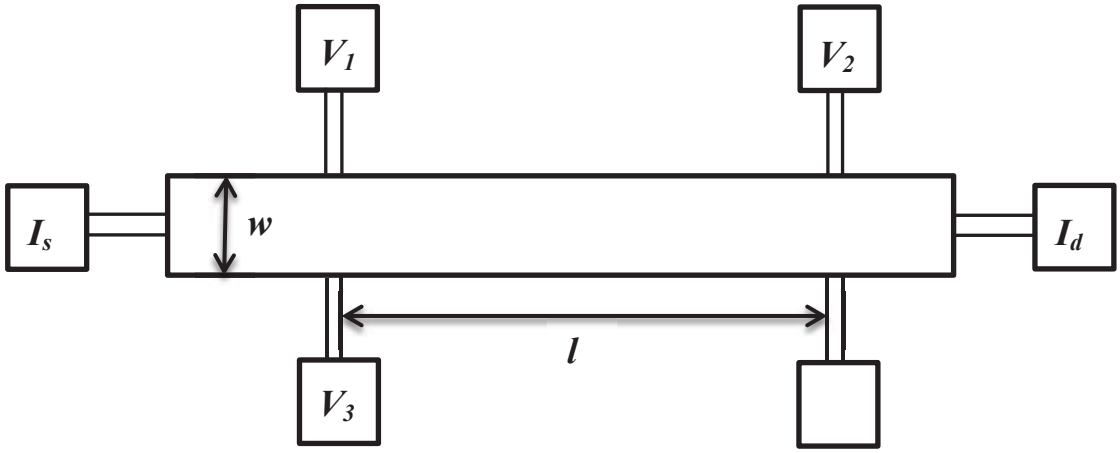

FIG. 3 Top of a Hall bar with width w and length l defined, with the number of squares being l/w. Both ac and dc currents are sent from the source, I_s, to the drain, I_d. The longitudinal resistance can be measured between contacts V_1 and V_2, while the Hall voltage can be measured from V_1 to V_3.

defined in the Hall bar than the VdP, making the Hall bar better suited for obtaining a high quality four terminal measurement. We perform four terminal measurements using the standard low frequency lock-in amplifier technique. For this technique we send an ac excitation current $i \approx 1$ μA through our sample and can then measure the Hall voltage and the longitudinal voltage. Since we are interested in measuring the sheet resistance (resistance per square) we make sure that we remain in the Ohmic region. For some measurements we will want to measure differential resistance, which we will only do on the Hall bar geometries. To do this measurement, we apply a dc current I along the same path as the excitation/measurement current. Then we get differential resistance as long as $I \gg i$.

Another lock-in technique will be utilized to directly measure photoresistance, $\delta\rho_\omega$, which is the magnetoresistance under the effects of microwave irradiation, ρ_ω, minus the magnetoresistance without microwave irradiation, ρ. We can express this relationship by: $\delta\rho_\omega = \rho_\omega - \rho$. To do this requires two lock-in amplifiers which have synchronized oscillators (Zudov, 1999). One lock-in amplifier provides the excitation current in the sample at frequency $2f$ while the other lock-in amplifier is used to chop or modulate the microwaves at frequency f. Once this is done, the photoresistance

can be measured on the Y-channel of the lock-in amplifiers.

II. SHUBNIKOV-DE HAAS OSCILLATIONS

Approximately 90 years ago, Shubnikov-de Haas Oscillations (SdHOs) were first observed (Shubnikov and de Haas, 1930), and despite having been studied for 9 decades, they are still studied today. During the studies of 2DEGs in this thesis, SdHOs will be looked at to gain some understanding of 2DEG systems. Namely, we will use them to look at the quantum scattering time τ_{q} and carrier density n_e. Also, we will show how one can use SdHOs to obtain effective mass $m^\star$ which is commonly done, though will not be done in this thesis. Here, a theoretical description of these oscillations along with the method to extract the desired parameters and notations that will be used throughout this thesis are presented.

A. SdHO Theory

SdHOs are oscillations that occur in the normalized resistivity, so we will start by deriving the normalized resistivity from the conductivity. The conductivity is expressed as and integration over energy through

$$\sigma \equiv \sigma_0 \int d\varepsilon \nu^2(\varepsilon) \left[-\partial_\varepsilon f(\varepsilon)\right] \tag{19}$$

where σ_0 is the Drude conductivity, $\nu(\varepsilon)$ is the density of states, and $f(\varepsilon)$ is the Fermi distribution function. Assuming overlapping Landau levels, as done previously, the DOS given in Eq. (17) can be simplified to its first harmonic under which it has the form (Dmitriev et al., 2012)

$$\nu(\varepsilon) = 1 - 2\lambda \cos\left(\frac{2\pi\varepsilon}{\hbar\omega_{\mathrm{c}}}\right) \tag{20}$$

where $\omega_{\mathrm{c}} = eB/m^\star$ is the cyclotron frequency with $m^\star$ denoting the effective mass of the charge carriers and λ is defined in Eq. (18). Using this form for the DOS, The conductivity expression can be evaluated:

$$\sigma = \sigma_0 \int d\varepsilon \left[1 - 4\lambda \cos\left(\frac{2\pi\varepsilon}{\hbar\omega_{\mathrm{c}}}\right) + 4\lambda^2 \cos^2\left(\frac{2\pi\varepsilon}{\hbar\omega_{\mathrm{c}}}\right)\right] \left[-\partial_\varepsilon f(\varepsilon)\right]. \tag{21}$$

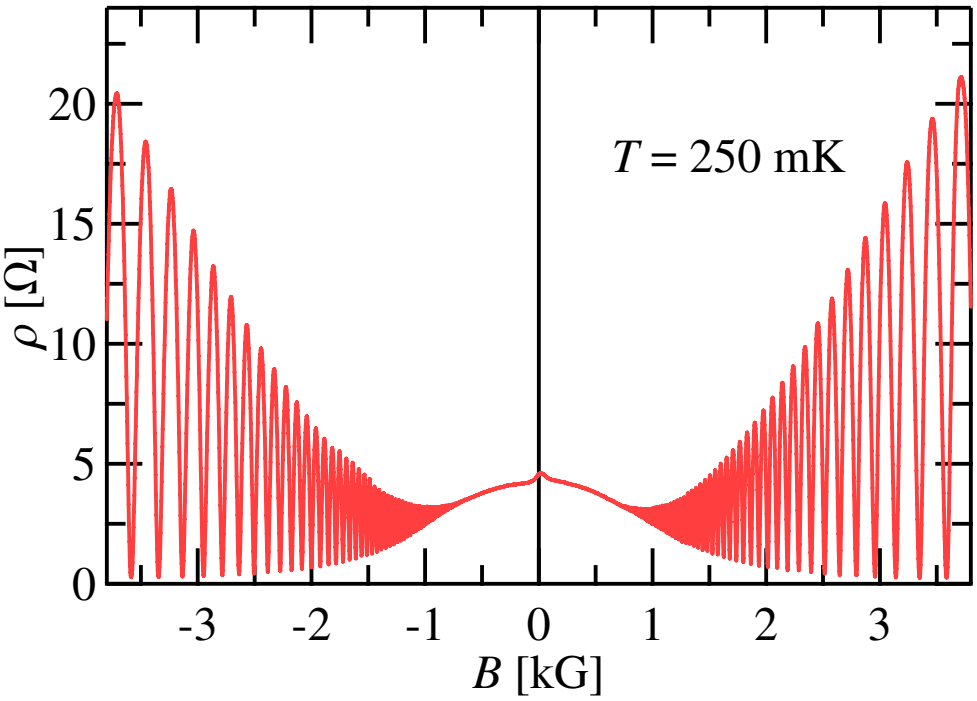

FIG. 4 [Adapted from (Hatke, 2011)] Magnetoresistivity measured at a temperature of $T = 250$ mK. The amplitude and spacing between the oscillations increases as the field increases. ($n_e = 2.43 \times 10^{11}$ cm^{-2} and $\mu = 5.2 \times 10^6$ cm^2/Vs)

This yields both a non-oscillatory correction and an oscillatory correction. The non-oscillatory correction is given approximately by

$$\sigma \simeq \sigma_0 \left(1 + 2\lambda^2\right). \tag{22}$$

The oscillatory correction is what is known as Shubnikov-de Haas oscillations and can be expressed as (Dmitriev et al., 2012)

$$\frac{\delta\sigma}{\sigma_0} \simeq \frac{\delta\rho}{\rho_0} = -4\lambda \frac{2\pi^2 k_\mathrm{b} T/\hbar\omega_\mathrm{c}}{\sinh\left(2\pi^2 k_\mathrm{b} T/\hbar\omega_\mathrm{c}\right)} \cos\left(\frac{2\pi E_F}{\hbar\omega_\mathrm{c}}\right). \tag{23}$$

In Fig. 4 an example of SdHOs is shown by plotting the magnetoresistivity ρ against magnetic field B measured at a fixed temperature of $T = 250$ mK. Starting from low magnetic field, ρ decreases until the onset of the SdHOs, which are the oscillations that grow in amplitude as the magnetic field increases.

Recall that the energy level spectrum has been quantized with the allowed electron energies being $E \simeq \hbar\omega_\mathrm{c}(N + 1/2)$, which leads to an oscillating density of states described in Eq. (17). Since the Fermi energy is fixed based on the carrier density, by

sweeping the magnetic field, the Fermi energy is swept through the energy level spectrum yielding a maximum (minimum) in the resistivity when the DOS is a minimum (maximum).

B. SdHO: Density and τ_{q}

The number filled LLs is known as the filling factor, $\nu = 2E_F/\hbar\omega_{\mathrm{c}}$. In this notation, Eq. (23) can be rewritten as

$$\delta\rho = -4\rho_0 D_T \lambda \cos(\pi\nu)\,,\ D_T = \frac{X_T}{\sinh(X_T)} \tag{24}$$

where $X_T = 2\pi^2 k_{\mathrm{b}} T m^\star \nu/\hbar h n_e$. By expressing SdHOs this way, one now has a method of directly obtaining the carrier density from the magnetoresistivity. This is accomplished by converting B into ν, an example of which is shown in the main part of Fig. 5. In this figure it is readily seen that minima (maxima) of the oscillations occur at even (odd) values of ν. Another way that is quicker but tends to be less accurate is to choose two minima and calculate $\nu_n - \nu_m$ using the two B field locations at which the two minima occur.

Now we can discuss how to use SdHOs to get τ_{q}. While this has become commonplace in the field to obtain this parameter from the Dingle factor (Coleridge et al., 1989), we will review the procedure. One first extracts the amplitude of the oscillations from the main portion of Fig. 5. Then one normalizes the amplitude by dividing by the zero-field resistivity ρ_0 and the magnetic field dependence, which is found in D_T. This yields the expression

$$\frac{\delta\rho}{\rho_0 D_T} = 4\lambda = 4\exp\left(\frac{\pi m^\star \nu}{h n_e \tau_{\mathrm{q}}}\right). \tag{25}$$

This normalized amplitude plotted on a log scale against ν is depicted in the inset of Fig. 5. The line passing through the points is the fit, which has its intercept at the expected value of 4. Then from the slope of the line we get $\tau_{\mathrm{q}} = 3.75$ ps. Likewise, one could also take the natural log of both sides, which would result in one not having to plot on a log scale, the intercept being $\ln(4)$, and the slope still yielding τ_{q}. One thing that must be remembered when getting this result is that SdHOs will result in an underestimate for τ_{q} due to macroscopic density fluctuations in the sample.

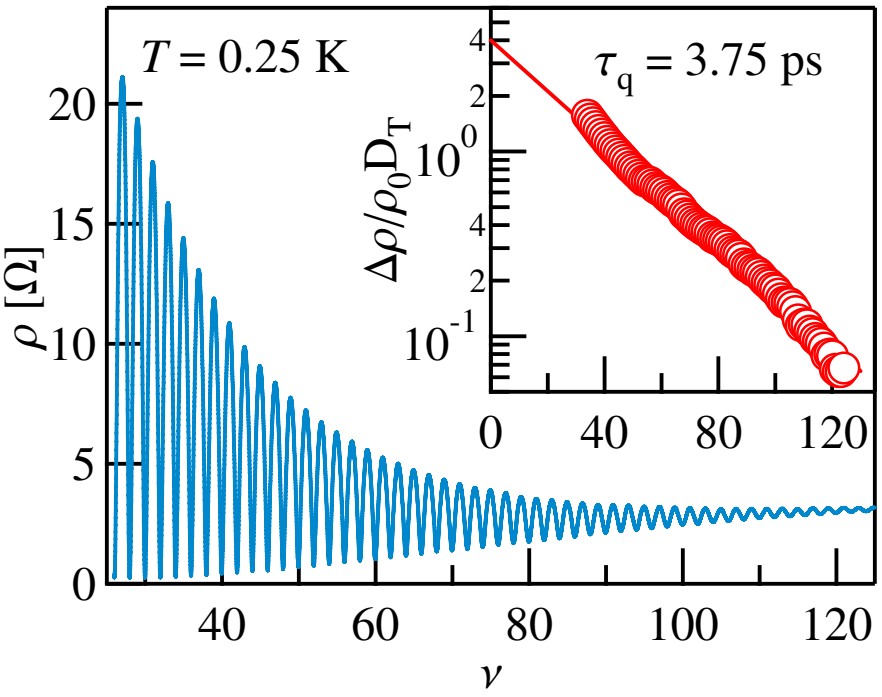

FIG. 5 [Adapted from (Hatke, 2011)] Main: Magnetoresistivity plotted as a function of the filling factor ν as a method for obtaining the carrier density. Inset: Normalized amplitude extracted as a function of ν used to obtain an estimate of the quantum scattering time $\tau_{\rm q}$. ($n_e = 2.43 \times 10^{11}$ cm^{-2} and $\mu = 5.2 \times 10^6$ cm^2/Vs)

C. SdHO: Effective Mass

Next, we will look at how to obtain $m^\star$ from temperature dependence of SdHO, specifically we will extract it from D_T. In the main part of Fig. 6 we plot SdHOs at various temperatures ranging from 0.25-2 K as a function of ν. The amplitude decreases as the temperature increases as is expected. Then choose a filling factor to get the amplitude at for each temperature; note that this is the same filling factor for each temperature. In the analysis depicted in the inset of Fig. 6, the amplitude normalized by its corresponding temperature at $\nu = 34$ is plotted on a log scale against temperature along with a fit line. The slope of the fit line coincides with the exponential of the hyperbolic sine function and yields a direct measurement of the effective mass. In this case we get an effective mass of $m^\star = 0.067m_0$, the standard effective mass for GaAs.

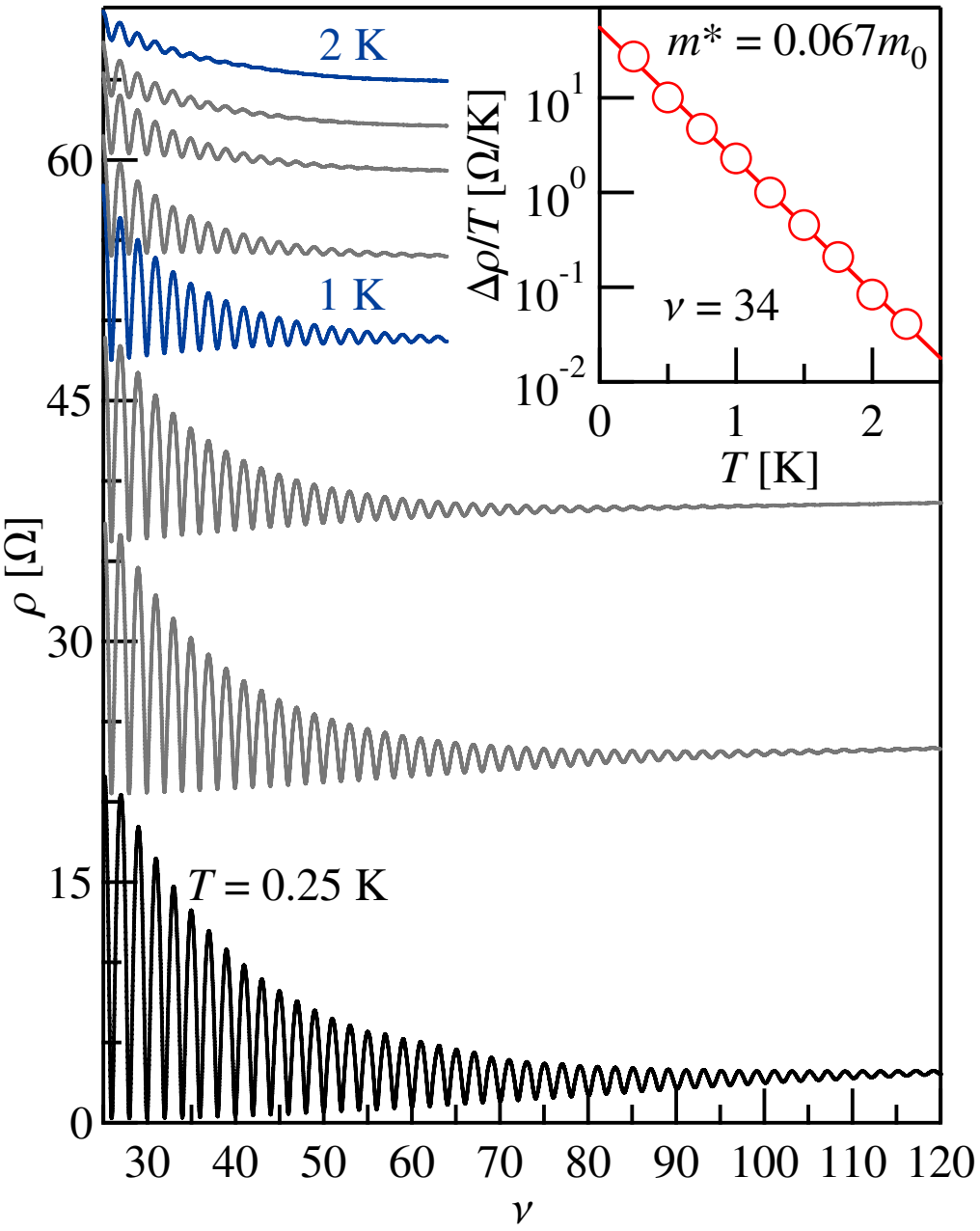

FIG. 6 [Adapted from (Hatke, 2011)] Main: Magnetoresistivity obtained at fixed temperatures of $T = 0.25 - 2$ K as a function of ν. Traces are vertically offset for clarity. Inset: Normalized amplitude, for $\nu = 34$, extracted as a function of T used to obtain an estimate of the effective mass of the charge carriers. ($n_e = 2.43 \times 10^{11}$ cm^{-2} and $\mu = 5.2 \times 10^6$ cm^2/Vs)

III. MICROWAVE INDUCED RESISTANCE OSCILLATIONS

Almost two decades ago, another oscillation in the longitudinal resistivity of 2DEGs known as microwave induced resistance oscillations (MIRO) were first observed (Ye et al., 2001; Zudov et al., 2001). These oscillations occur when a 2DEG with sufficiently high mobility ($\mu > 10^6$ cm^2/Vs) is subjected to microwave illumination and a weak magnetic field. In this introduction to MIRO, this thesis will look first at MIRO from an experimental results view, then look at the current theory behind this phenomena. From the theory, it will be shown MIRO allows one to extract parameters similar to those that were obtained from SdHO.

A. Experimental Observations

MIROs are often seen at lower magnetic fields than SdHOs, as can be seen in Fig. 7 where MIRO are the large oscillations and SdHOs are the small oscillations that start appearing just below 2 kG. Similar to SdHO, the amplitude of MIRO decreases as the magnetic field decreases. With the various similarities to SdHO, it was quickly determined that there is an order parameter, $\epsilon_{\rm ac}$, for the oscillations that is the ratio of the microwave frequency, ω, and the cyclotron frequency, $\omega_{\rm c}$,

$$\epsilon_{\rm ac} \equiv \frac{\omega}{\omega_{\rm c}} = \frac{2\pi f m^\star}{eB} \tag{26}$$

Here the period is seen to be proportional to the effective mass and inversely proportional to the magnetic field. Plotted in Fig. 8 is the magnetoresistivity vs $\epsilon_{\rm ac}$, with the integer values of $\epsilon_{\rm ac}$ indicated by vertical lines. As can be seen here, the maxima(+) and minima(-) are not located at the integer values of $\epsilon_{\rm ac}$, but instead are equally offset from the integer values of $\epsilon_{\rm ac}$ by a common phase, $\phi \approx 1/4$. Thus, one can express the locations of the maxima and minima by

$$\epsilon_{\rm ac}^{\pm} = n \mp \phi, \quad n = 1, 2, 3, \ldots \tag{27}$$

where we call n the order of the oscillation. This method of describing MIRO leads to simpler and more intuitive methods of finding $m^\star$ than in SdHO. To find the effective mass, one way is to simply plot the magnetoresistivity as a function of $\epsilon_{\rm ac}$ similar

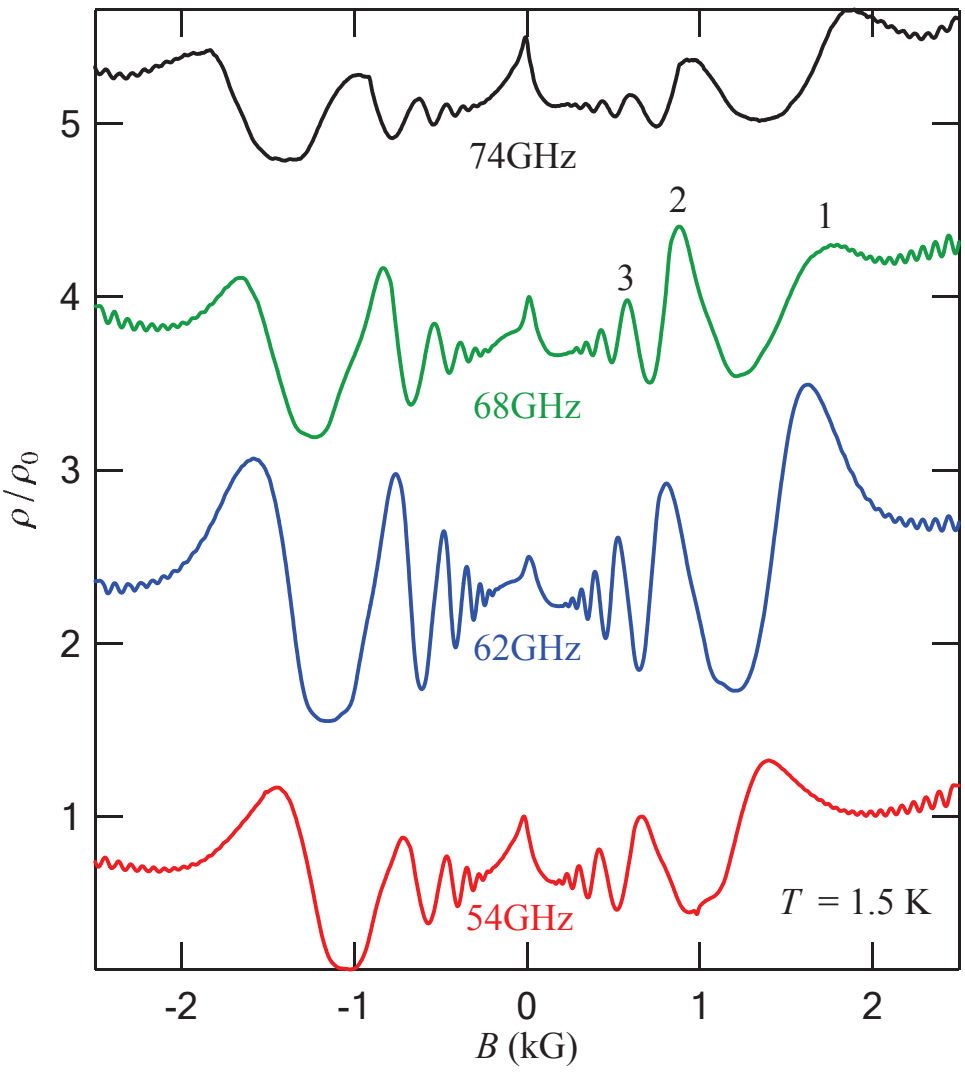

FIG. 7 Magnetoresistivity with microwave irradiation plotted against magnetic field for frequencies f =54, 62, 68, and 74 GHz normalized to their value at $B = 0$. The numbers above the 68 GHz oscillations indicate the oscillation number according to the ordering parameter, $\epsilon_{\rm ac}$. The data was obtained at $T \approx 1.5$ K in a 200 μm wide Hall bar sample with ($n_e = 3.5 \times 10^{11}$ cm^{-2} and $\mu = 5.6 \times 10^6$ cm^2/Vs).

to what is seen in Fig. 8. Since the frequency and magnetic field are known at each point, one only needs to adjust $m^\star$ until the maxima/minima are properly aligned to determine the value of $m^\star$. Another method is to plot B^{-1} for each extrema as a function of $\epsilon_{\rm ac}$ and fit to a line yielding $slope = 2\pi/m^\star$. When using MIRO to obtain $m^\star$, the effective mass is found to be $m^\star \approx 0.063m_0$ for our GaAs 2DEGs, which is slightly lower than the value of $m^\star = 0.067m_0$ found from SdHO.

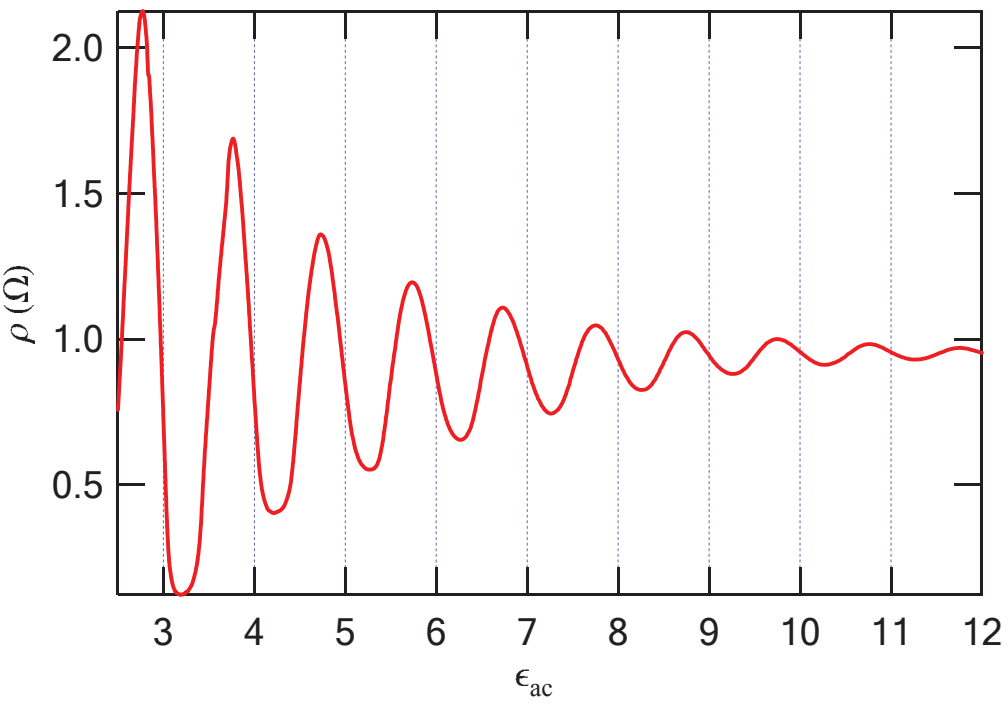

FIG. 8 Magnetoresistivity as a function of $\epsilon_{\rm ac}$ with integer values of $\epsilon_{\rm ac}$ indicated by dashed vertical lines. The maxima and minima are evenly displaced from the integer values by $\phi \approx 0.25$. The data was obtained at $T \approx 0.29$ K in a 4x4 mm VdP sample with ($n_e = 2.6 \times 10^{11}$ cm^{-2} and $\mu = 29.7 \times 10^6$ cm^2/Vs).

Making further use of MIROs similarity to SdHOs, the amplitude being related to the Dingle factor was also found; however we will delay looking in detail at this relation until we look at the theoretical background of MIRO beginning with the mechanisms that allow this phenomena to manifest.

B. MIRO Theoretical Results

MIROs have been theoretically understood through two competing models known as the displacement mechanism (Dmitriev et al., 2009; Durst et al., 2003; Lei and Liu, 2003; Ryzhii, 1970; Vavilov and Aleiner, 2004) and the inelastic mechanism (Dmitriev et al., 2009, 2005). The displacement mechanism is best described as the shift of the cyclotron orbit center due to microwave-assisted impurity scattering. By this we mean that an electron in the sample first is excited by absorbing a photon, thus causing that electron to transition between LLs as depicted in Fig. 9. After this energy transition,

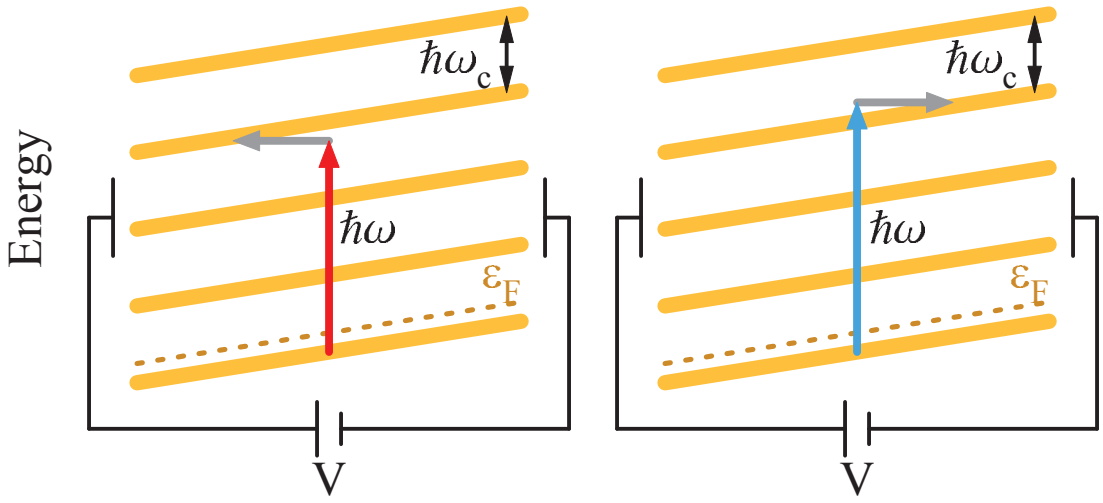

FIG. 9 Cartoon depicting the displacement model. The yellow lines are the LLs tilted by an applied excitation voltage, and the blue and red arrows represent the transition that occurs from the absorption of a photon by an electron. The electron then scatters off an impurity into a LL, represented by the gray arrow transitions. The LLs are offset from one another by $\hbar\omega_c$ and the transition depicted in the right (left) of the plot is for a MIRO minima (maxima).

the electron then scatters off an impurity into one of the adjacent LLs which has been tilted by an applied excitation voltage. When the electron scatters off an impurity when it is just above (below) a LL, it scatters forward (backward) creating a minima (maxima) in the resistance. The inelastic mechanism comes from a radiation induced change in the electron distribution function.

Both of these mechanisms predict that the photoresistivity oscillates as (Dmitriev et al., 2009, 2005; Durst et al., 2003; Lei and Liu, 2003; Ryzhii, 1970; Vavilov and Aleiner, 2004)

$$\frac{\delta\rho_\omega}{\rho_0} = -2\pi\eta\mathcal{P}_\omega\lambda_\omega^2\epsilon_{\rm ac}\sin 2\pi\epsilon_{\rm ac} \tag{28}$$

where η is the dimensionless scattering rate, $\mathcal{P}_\omega$ is the dimensionless microwave power (Dmitriev et al., 2005; Khodas and Vavilov, 2008), $\lambda_\omega = \exp(-\pi/\omega_c\tau_{q,\,\omega})$ is the Dingle factor similar to what is seen in the SdHO section, and $\tau_{q,\,\omega}$ is the quantum scattering time obtained when microwaves are present. Since $\delta\rho_\omega \propto \sin 2\pi\epsilon_{\rm ac}$, this confirms the previous method described for using MIRO to find the effective mass of a sample is accurate. For the displacement mechanism, $\eta = \tau/2\tau_\star$ where $\tau_\star$ is a scattering

time characterizing the correlation properties of the disorder potential, while for the inelastic mechanism $\eta = 2\tau_{\rm in}/\tau$ where $\tau_{\rm in}$ is the inelastic scattering time. The main difference between the two mechanisms is their proportionality to different scattering times. This difference is most prominent in the fact that for the displacement mechanism, η is temperature independent, while for the inelastic mechanism, $\eta \propto T^{-2}$. The temperature dependence for the inelastic mechanism comes from $\tau_{\rm in} \simeq \tau_{\rm ee} \propto T^{-2}$ (Dmitriev et al., 2003, 2005; Giuliani and Quinn, 1982).

1. MIRO Temperature Dependence and Quantum Lifetime

There are two places in Eq. (28) that have temperature dependence: the Dingle factor and the dimensionless scattering rate.

The difference between the Dingle factor for MIRO and the Dingle factor for SdHO is found in $\tau_{\rm q}$. For SdHO, $\tau_{\rm q}$ is only from a temperature independent contribution that is attributed to impurities given by

$$\frac{1}{\tau_{\rm q}} = \frac{1}{\tau_{\rm q}^{\rm im}} \tag{29}$$

In contrast to this, the $\tau_{{\rm q},\,\omega}$ in MIRO has the same contribution from impurities and an additional temperature dependent contribution arising from electron-electron interactions (Hatke et al., 2009a,b,c) which we relate by

$$\frac{1}{\tau_{{\rm q},\,\omega}} = \frac{1}{\tau_{\rm q}^{\rm im}} + \frac{1}{\tau_{\rm q}^{\rm ee}}, \qquad \frac{1}{\tau_{\rm q}^{\rm ee}} \simeq \kappa \frac{T^2}{E_F} \tag{30}$$

where κ is a dimensionless constant.

Thus, while both mechanisms predict the same temperature dependence in the Dingle factor, they predict differing temperature dependencies in the dimensionless scattering rates. None the less, since for both mechanisms the photoresistivity is proportional to the square of the same Dingle factor, one can use a method to find $\tau_{{\rm q},\,\omega}$ nearly identical to that seen in SdHO to find $\tau_{\rm q}$. To find $\tau_{{\rm q},\,\omega}$ one creates a Dingle plot by plotting $\ln(\delta\rho_\omega/\rho_0\epsilon_{\rm ac})$ vs $\epsilon_{\rm ac}$ and can extract the temperature dependent $\tau_{{\rm q},\,\omega}$ from the slope. The $\tau_{{\rm q},\,\omega}$ from MIRO will always be much larger than $\tau_{\rm q}$ from SdHO. This arises from SdHO being sensitive to macroscopic density fluctuation, while MIRO

are robust against such fluctuations. Thus we have a good method for obtaining $\tau_{\mathrm{q},\,\omega}$ from MIRO.

To determine the dominant scattering mechanism, one looks at the temperature dependence of the intercept of the Dingle plots. By plotting the intercepts of the Dingle plots against T^{-2} and observing the behavior, it will either be linear (inelastic mechanism dominates) or approximately constant (displacement mechanism dominates). Another less rigorous method that can be used if Dingle plots are not available due to sufficiently low $\tau_{\mathrm{q},\,\omega}$ is to choose a maxima/minima and plot the amplitude against T^{-2} and observe the behavior. A linear relationship shows the inelastic mechanism to be dominant while a constant amplitude indicates the displacement mechanism is dominant.

2. MIRO: Effective Mass

There are three methods for finding effective mass from MIRO. The first two are to plot photoresistivity or magnetoresistivity against ϵ_{ac} or B^{-1} for each extrema against ϵ_{ac} as described in Sec III.A.

Eq. (28) gives rise to the second method for obtaining the effective mass, which is referred to as the fan diagram method. For this method, one simply needs to pick a maxima/minima and measure the magnet field location for the chosen extrema at several frequencies. Then by plotting f vs the magnetic field location of the chosen maxima/minima at each frequency and fitting that data to a line, one can extract $m^\star$ from the slope.

The effective mass in MIRO is often observed to be less than that observed in SdHO. In MIRO, $m^\star$ between $0.061m_0$ and $0.063m_0$ are not uncommon values to be observed. Evidence that this suppression is attributed to electron-electron interactions (Hatke et al., 2013) where $m^\star \approx 0.059m_0$ has been observed, and depending on carrier density, $m^\star$ can either increase or decrease (Asgari et al., 2005; Asgari and Tanatar, 2006; Coleridge et al., 1996; Drummond and Needs, 2009; Kwon et al., 1994; Smith et al., 1992; Tan et al., 2005; Zhang and Das Sarma, 2005).

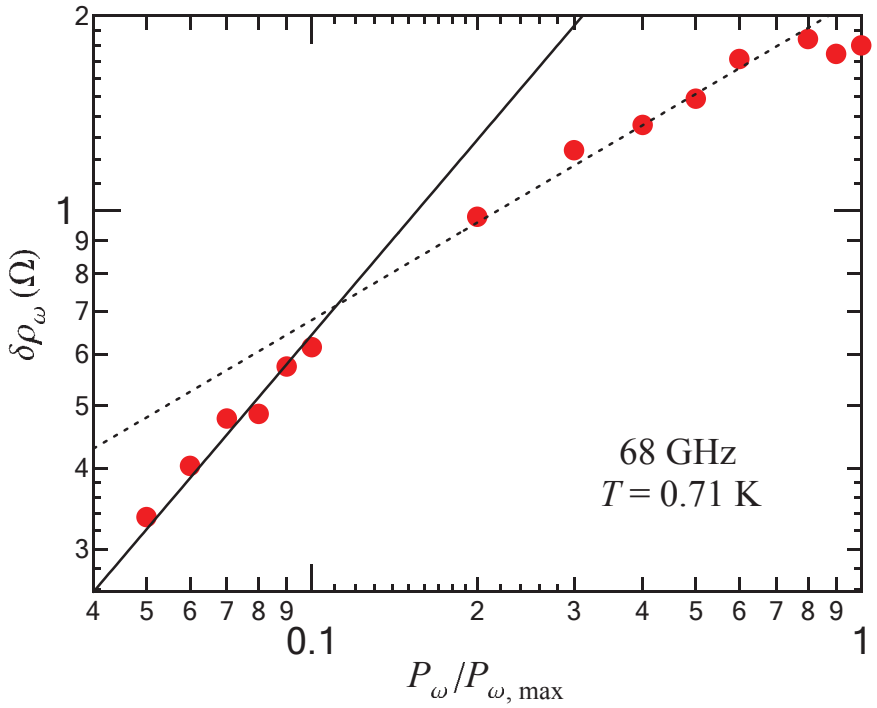

FIG. 10 MIRO amplitude, $\delta\rho_\omega$ as a function of normalized applied microwave power for $f = 68$ GHz. The solid line represents $\delta\rho_\omega \propto \mathcal{P}_\omega$ while the dotted line represents $\mathcal{P}_\omega^{0.5}$ behavior. The data was obtained at $T \approx 0.71$ K in a Hall bar sample with ($n_e = 2.5 \times 10^{11}$ cm^{-2} and $\mu = 23.7 \times 10^6$ cm^2/Vs).

3. MIRO: Power Dependence

The last topic regarding MIRO behavior to be covered here is power dependence of the amplitude. Theoretically, Eq. (28) predicts a linear power dependence, $\delta\rho_\omega \propto \mathcal{P}_\omega$; however, further studies have shown that with increasing $\mathcal{P}_\omega$, the linear dependence crosses over to a square-root dependence, $\delta\rho_\omega \propto \sqrt{\mathcal{P}_\omega}$, which arises from microwave absorption saturation effects (Dmitriev et al., 2005; Hatke et al., 2011a) or the increase of multi-photon processes (Hatke et al., 2011a; Khodas et al., 2010; Khodas and Vavilov, 2008). Experimentally this crossover has been observed (Hatke et al., 2011a), but there are also several experiments that have observed only sub-linear power dependence with a range of exponents (Mani et al., 2010, 2004; Studenikin et al., 2004; Ye et al., 2001). Fig. 10 depicts this crossover by plotting the MIRO amplitude, $\delta\rho_\omega$, as a function of normalized applied microwave power, $\mathcal{P}_\omega/\mathcal{P}_{\omega,\,\mathrm{max}}$, under irradiation at $f = 68$ GHz. The solid black line shows the linear power depen-

dence while the dotted line indicates the sub-linear power dependence that is expected at higher power.

IV. HALL FIELD-INDUCED RESISTANCE OSCILLATIONS

Another class of magnetoresistance oscillations can occur in a 2DEG's longitudinal differential resistance, r, is called Hall field-induced resistance oscillations (HIRO). This occurs when the 2DEG is subjected to a weak magnetic field and a dc current, I, that is applied along the same path as the ac measurement current, i, used in standard lock-in techniques with $I \gg i$. This phenomena will directly be presented through its theoretical description.

A. HIRO Theory

HIRO is explained through the same displacement mechanism as was seen in MIRO, except where MIRO was a result of transitions occurring from the electrons absorbing photons, HIRO occurs due to the drift motion of the electrons from I opening a new set of scattering events that can occur from electrons scattering off of impurities (Lei, 2007; Vavilov et al., 2007).

For $2\pi\epsilon_j \gg 1$, the expression for the correction to the differential resistance takes the form: (Dmitriev et al., 2012)

$$\frac{\delta r}{\rho_0} = \frac{16}{\pi}\frac{\tau}{\tau_\pi}\lambda_\omega^2 \cos(2\pi\epsilon_j) \tag{31}$$

where τ_π is the back-scattering time, λ_ω is the same temperature dependent Dingle factor as seen in MIRO, $\epsilon_j = eE(2R_c)/\hbar\omega_c$ is the HIRO ordering parameter, $2R_c$ is the cyclotron diameter, $E = j\rho_H$ is the Hall electric field, j is the current density, and ρ_H is the Hall resistance. This expression has been successfully applied to understand HIRO in past studies (Bykov et al., 2007; Hatke et al., 2010, 2009b, 2011b; Shi et al., 2014; Zhang et al., 2008). A more useful form of ϵ_j for analyzing/extracting information from HIRO is as follows:

$$\epsilon_j = j\frac{2m^\star}{Be^2}\sqrt{\frac{2\pi}{n_e}} \tag{32}$$

This form is more useful because it is expressed explicitly in terms of effective mass, which is one of the parameters we are interested in using HIRO to understand. In all the samples that will be analyzed in this thesis, $\tau_\pi \simeq \tau_{\rm sh}$ (Khodas and Vavilov, 2008).

Plotted in Fig. 11 is the differential resistance normalized by the Drude resistance plotted against magnetic field for various currents with vertical offsets. As the current

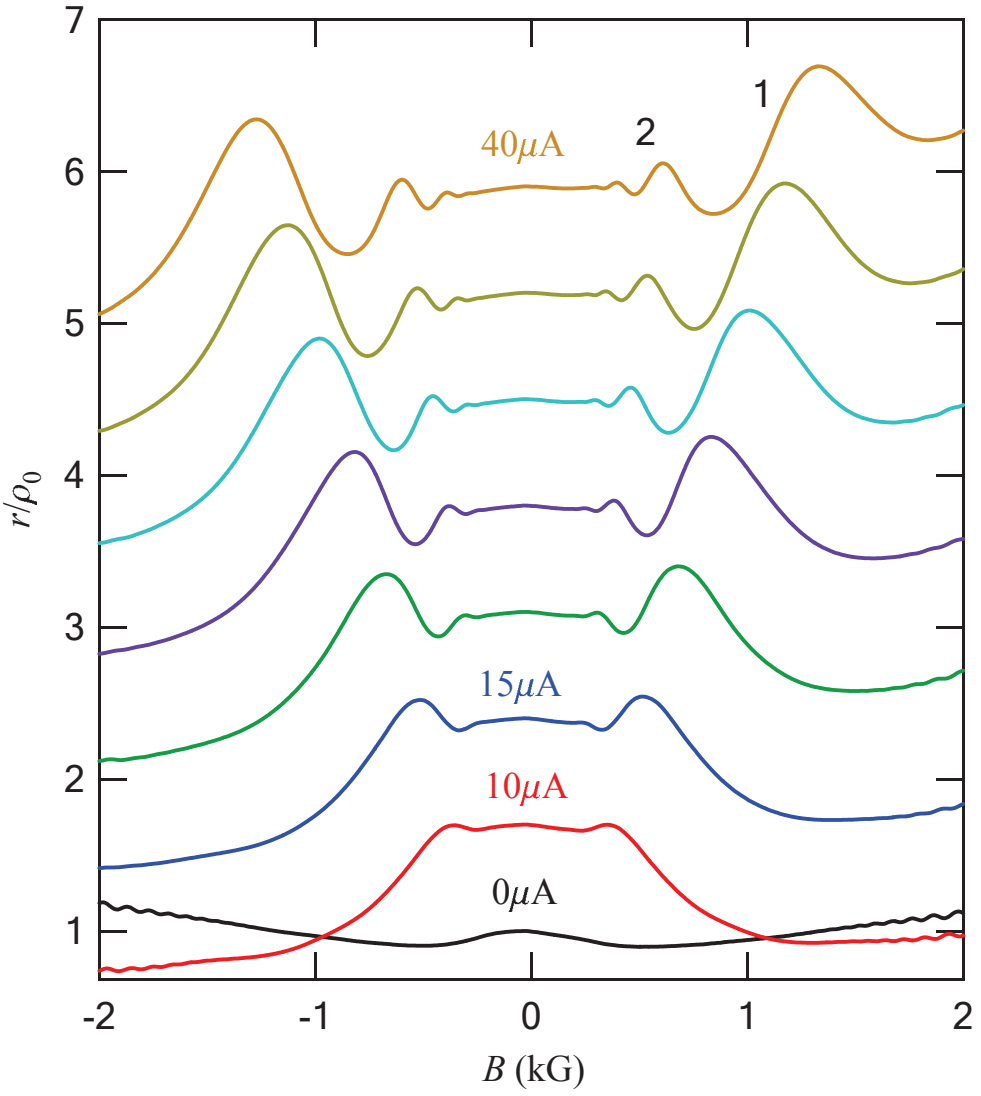

FIG. 11 Normalized differential resistance, r, plotted against magnetic field, B, plotted with an offset for no dc current and dc currents 10-40 μA in steps of 5 μA. Ordering of oscillations is indicated by numbers above the 40 μA data. The data was obtained at $T \approx 1.5$ K in a 100 μm wide Hall bar with ($n_e = 1.57 \times 10^{11}$ cm^{-2} and $\mu = 4.6 \times 10^6$ cm^2/Vs).

increases, the large low field oscillations are the HIRO and they increase in size and move to larger magnetic fields. The small oscillations that appear above 1.5 kG in the lower current traces are SdHOs. Since HIRO goes as $\cos(2\pi\epsilon_j)$, the maxima (minima) will occur at integer (half-integer) values of ϵ_j as seen in Fig. 12.

One may think that HIRO would be useful for finding density since ϵ_j is dependent on density, but if one gets density from HIRO, they need to get effective mass from somewhere else since one is needed to find the other. We consider it more useful to use other methods for finding density (SdHOs and the Hall effect) because when finding effective mass from other methods there are still questions that need to be better understood; for example, the disparity between the effective mass of MIRO and SdHO.

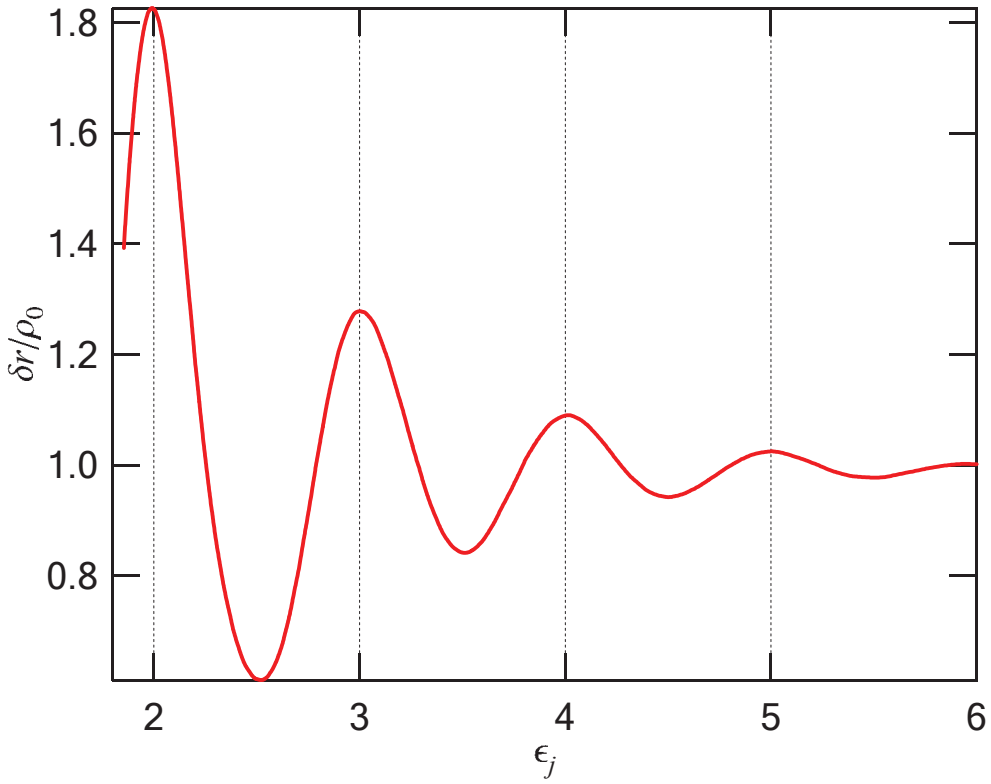

FIG. 12 Normalized differential resistance as a function of ϵ_j with an applied current of 150 μA at $T \approx 1.5$ K. The periodicity of HIRO with ϵ_j is clearly shown, with maxima at integer values. The data was obtained in a 300 μm wide Hall bar with ($n_e = 2.82 \times 10^{11}$ cm^{-2} and $\mu = 4.52 \times 10^6$ cm^2/Vs).

B. HIRO: Effective Mass and Quantum Lifetime

As with SdHO and MIRO, HIRO is also useful for finding effective mass and quantum scattering time. To find effective mass, there are two useful methods one can apply, the first of which is to plot normalized differential resistance as a function of ϵ_j, which is similar to how effective mass was found using MIRO. The other method requires several different currents such as in Fig. 11, and then by choosing an integer (half-integer) value of ϵ_j you plot B vs I for the chosen maximum (minimum) at various currents. Then, by directly applying the slope of the line formed to Eq. (32), the definition of ϵ_j, one gets the effective mass. Effective mass values found from HIRO data are the same as those from MIRO, $m^\star \simeq 0.063 m_0$, thus having a lower effective mass than found from SdHO.

Quantum scattering time is determined through a Dingle analysis similar to how it was done with MIRO, except plotting $\ln(\delta r/\rho_0)$ vs B^{-1} to get the needed slope.

Part II

Experimental Investigations

V. GERMANIUM

For nearly 2 decades, MIRO and HIRO have only been observed in n-type GaAs/AlGaAs. Measurements of microwave photoresistance in p-type GaAs/AlGaAs (Du et al., 2004), n-type Si/SiGe (Sassine et al., 2007), and HgTe/CdHgTe (Kozlov et al., 2011) found only a single photoresistance peak which was attributed to magneto-plasmon resonance (Vasiliadou et al., 1993). This thesis will show MIRO and HIRO measurements done in p-type Ge/SiGe, the second material to see these phenomena.

A. Strained Germanium Samples

We will be presenting data from two different Ge samples that are both modulation doped and fabricated through reduced pressure chemical vapor deposition (Dobbie et al., 2012). In both samples, holes are supplied by a 10 nm-wide Boron doped donor layer. The first sample is a 4 mm x 4 mm Van der Pauw (VdP) with hole density $n_e = 2.78 \times 10^{11}$ cm^{-2} and $\mu = 0.37 \times 10^6$ cm^2/Vs. It is a 20 nm wide, 99.99% pure Ge quantum well with a 30 nm spacer. The second sample is a 50 μm wide Hall bar with $n_h = 2.66 \times 10^{11}$ cm^{-2} and $\mu = 1.4 \times 10^6$ cm^2/Vs. The Hall bar sample has a 20 nm wide, 99.99% pure Ge quantum well with a 36 nm spacer.

B. MIRO in Ge

The majority of the experiments involving microwave irradiation done on the Ge samples were done on the VdP sample, so unless otherwise noted, all data shown is for the VdP sample in this MIRO section. First, we will establish that what is observed in this sample is indeed MIRO. The photoresistance, (δR_ω), is obtained by subtracting the magnetoresistance without microwave irradiation from the magnetoresistance with microwave irradiation, $\delta R_\omega = R_\omega - R$. Fig. 13 shows a typical photoresistance vs B as measured on the VdP sample. There is a set of fast oscillations that occur when $B > 3$ kG, which indicate a reduction to SdHO amplitude due to heating from the incident microwaves. There is also a second set of oscillations that go to lower

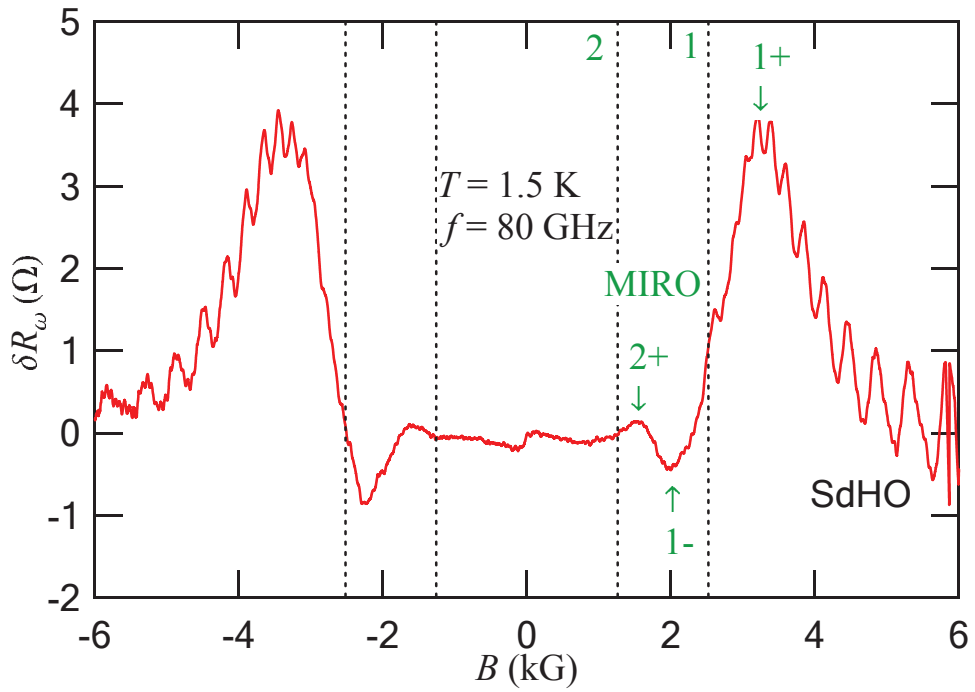

FIG. 13 Microwave photoresistance, δR_ω, as a function of magnetic field, B, measured at $T = 1.5$ K and $f = 80$ GHz. Vertical lines indicate $\epsilon_{\rm ac} = 1, 2$ as indicated by the green numbers at the top which were calculated using $m^\star = 0.088 m_0$.

field that have 2 maxima (marked by 1+, 2+) and 1 minima (marked by 1-).

A couple notable features of these oscillations is that first, the minima are actually negative, causing a decrease in the resistance of the sample, which is an important feature of MIRO. Another feature which is indicative of MIRO is found in the positions of the maxima and minima. As described by Eq. (27), the maxima and minima should be roughly equally offset from the integer values of $\epsilon_{\rm ac}$. As shown in Fig. 13, the photoresistance follows this behavior reasonably well when one uses an effective mass of $m^\star = 0.088 m_0$.

1. Frequency Dependence

Eq. (28) says that if one selects a maxima or minima and then increases the frequency, the location of the selected maxima/minima will shift to a higher B value. This behavior is evident in Fig. 14 (a) where the photoresistance as a function of magnetic field is plotted for various frequencies. So, for each peak, the B-field lo-

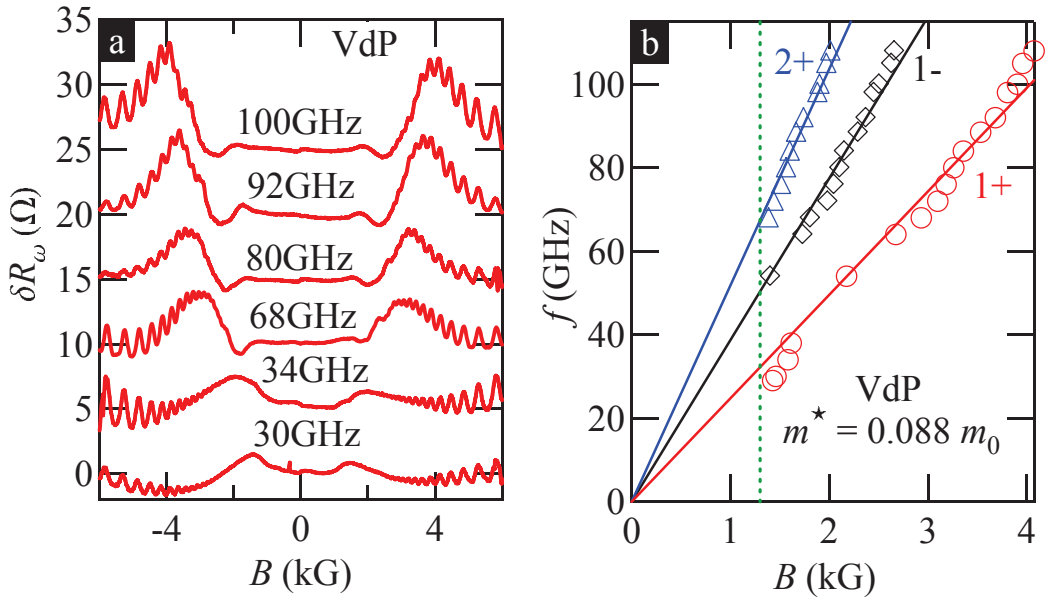

FIG. 14 (a) Microwave photoresistance, δR_ω, as a function of magnetic field, B, for various f. The location of the outermost peak clearly moves to higher B as f increases. (b) f vs B plotted for the maxima/minima (1+, 1-, 2+) that appear in the photoresistance traces. The linear fits were forced through the origin and were used to determine the effective mass to be $m^\star = 0.088m_0$. The vertical line indicates the lowest B at which MIRO appear, $B_c = 1.3$ kG.

cation was plotted at each frequency as illustrated in Fig. 14 (b). As can be seen, each maxima/minima (1+, 1-, 2+) can be fit to a line that passes through the origin, indicating the shifting of the extrema outward as f increases. From the slopes of these lines, we calculated that the effective mass of the holes in the Ge sample is $m^\star = 0.088m_0$. What has been observed so far is sufficient proof for claiming these oscillations to be manifestations of MIRO.

2. Quantum Lifetime in Ge

Another interesting feature of Fig. 14 (b) is that MIRO extrema do not appear at below a critical field, $B_c \simeq 1.3$ kG, indicated by the vertical dashed line. This holds true for all frequencies studied and for all orders of oscillations. We can use this critical field to create a rough estimate for the quantum lifetime. To do this we

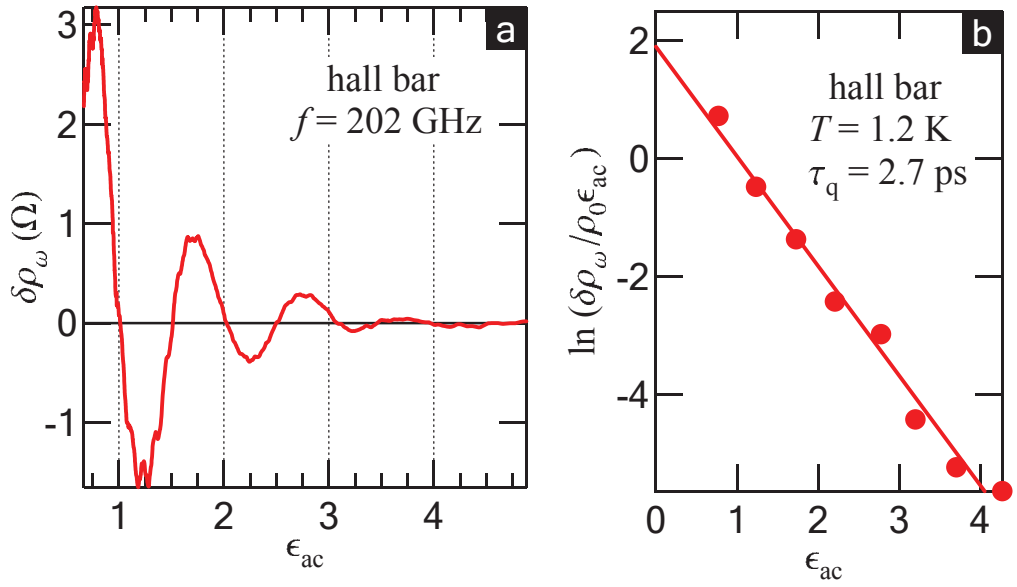

FIG. 15 (a) Microwave photoresistivity, δR_ω, as a function of the ordering parameter, ϵ_{ac}, for $f = 202$ GHz. Data taken on the Hall bar sample at temperature $T = 1.2$ K. (b) Dingle plot for MIRO trace shown in (a) which gives quantum lifetime $\tau_q = 2.7$ ps.

set $\omega_c\tau_q = 1$ at $B = B_c$, which gives $\tau_q = m^\star/eB_c \approx 4$ ps.

We also applied high frequency microwaves on the Hall bar sample, and have plotted $\delta\rho_\omega$ vs ϵ_{ac} in Fig. 15 (a). Here we can see almost 4 orders of oscillations with the maxima/minima appearing with the expected phase displacement of $\phi \approx 0.25$. Since this sample shows multiple oscillations, we are able to do a Dingle analysis to get the quantum lifetime $\tau_q = 2.7$ ps, shown in Fig. 15 (b). This value is comparable to the value estimated in the VdP sample.

3. Mechanisms and Temperature Dependence

Next we will see that the inelastic mechanism dominates over the range of temperatures studied, with all the temperature dependence data being taken on the VdP sample. Fig. 16 (a) shows δR_ω vs B for temperatures from 1-5 K in steps of 1 K with vertical offsets indicated by the horizontal dashed lines for clarity. The 1 K trace in green has a significant amount of SdHOs occurring in the MIRO range, thus we removed the SdHO contribution and have shown the photoresistance with no SdHOs as a black trace. As expected, the amplitude of MIRO decreases as the temperature

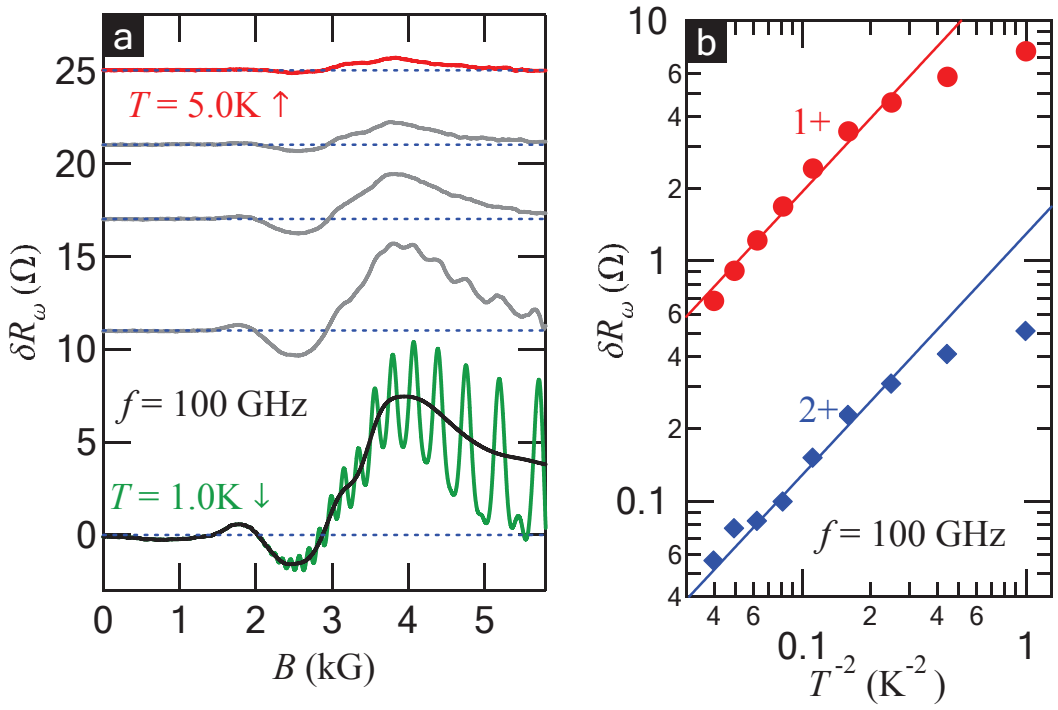

FIG. 16 (a) Microwave photoresistance with a vertical offset, δR_ω, as a function of the magnetic field, B, for temperature increasing from 1 K to 5 K in steps of 1 K as one goes from the bottom trace to the upper trace for $f = 100$ GHz. The 1 K (green) trace has a significant amount of SdHOs overlapping with the MIRO range, the black trace has had the SdHO contribution removed. (b) δR_ω vs T^{-2} for maxima 1+ (2+) indicated by the solid circles (diamonds). The solid lines represent $\delta R_\omega \propto T^{-2}$.

increases.

Fig. 16 (b) illustrates that the temperature dependence of the first two MIRO maxima behave as $\delta R_\omega \propto T^{-2}$. Recalling Eq. (28), there are two factors that have temperature dependence. The first factor comes from a carrier-carrier interaction correction to the quantum scattering rate, $\tau_{\mathrm{q},\,\omega}^{-1}$, (Hatke et al., 2009a,b,c) which appears in the Dingle factor, $\lambda_\omega = \exp(-\pi/\omega_c \tau_{\mathrm{q},\,\omega})$. This correction is of the order $\tau_{\mathrm{in}}^{-1} \sim T^2/E_F$. However, in our 2DHG, the impurity scattering rate is expected to be significantly larger, thus we don't expect this correction to cause a significant effect on $\tau_{\mathrm{q},\,\omega}$. Assuming $T = 4$ K, we estimate $\tau_{\mathrm{in}}^{-1} \approx 0.2$ K, which is a full order of magnitude smaller than the impurity contribution $\tau_{\mathrm{q},\,\omega}^{-1} \approx 2$ K.

Since the $\tau_{\mathrm{q},\,\omega}$ correction appears to be insignificant, we look at the dimensionless

scattering rate, η, which is the second factor that has T-dependence. Recalling that η has two contributions, the displacement and inelastic mechanisms, which we represent as: (Dmitriev et al., 2009)

$$\eta = \frac{\tau}{2\tau_\star} + \frac{2\tau_{\rm in}}{\tau} \tag{33}$$

where the first term comes from the displacement mechanism and the second term comes from the inelastic mechanism. The displacement contribution comes from the correlation properties of the disorder potential, and under the limit of sharp disorder (only impurities in the quantum well), $\tau/2\tau_\star = 3/2$. In the opposing limit of only smooth disorder (only from ionized acceptors in the donor layer), we get $\tau/2\tau_\star = 6\tau_{\rm q}/\tau$. Thus, we can express the contribution from the displacement mechanism by $\tau/2\tau_\star < 1.5$ for our sample.

The inelastic contribution is determined by the inelastic scattering time, $\tau_{\rm in} \sim E_F/T^2$, thus giving a larger contribution at low T. We estimate that at $T = 4$ K, $\tau_{\rm in} \approx 40$ ps giving a total inelastic contribution of $2\tau_{\rm in}/\tau \approx 4$ which leads us to suspect that the inelastic contribution should dominate over the temperature range where MIRO appear.

From what was said above, we expect the MIRO amplitude to decrease as T^{-2} as temperature increases. To verify our prediction, we plot MIRO amplitude δR_ω as a function of T^{-2} on a log-log scale where the circles (diamonds) represent the first (second) maxima. At high temperatures, we do indeed observe good agreement with the expected T^{-2} dependence, as indicated by the solid lines. However, at lower temperature, the data falls below the expected dependence which could be attributed to radiation induced heating of the 2DHG. Thus, we conclude that the temperature dependence of the oscillation amplitude of MIRO comes from the inelastic mechanism.

4. Power Dependence

Fig. 17 (a) shows microwave photoresistance, δR_ω, as a function of magnetic field, B, for applied microwave powers from 0 dB to 20 dB with $f = 38$ GHz and $T = 1.5$ K. At this frequency, the first MIRO maxima is observed with an amplitude

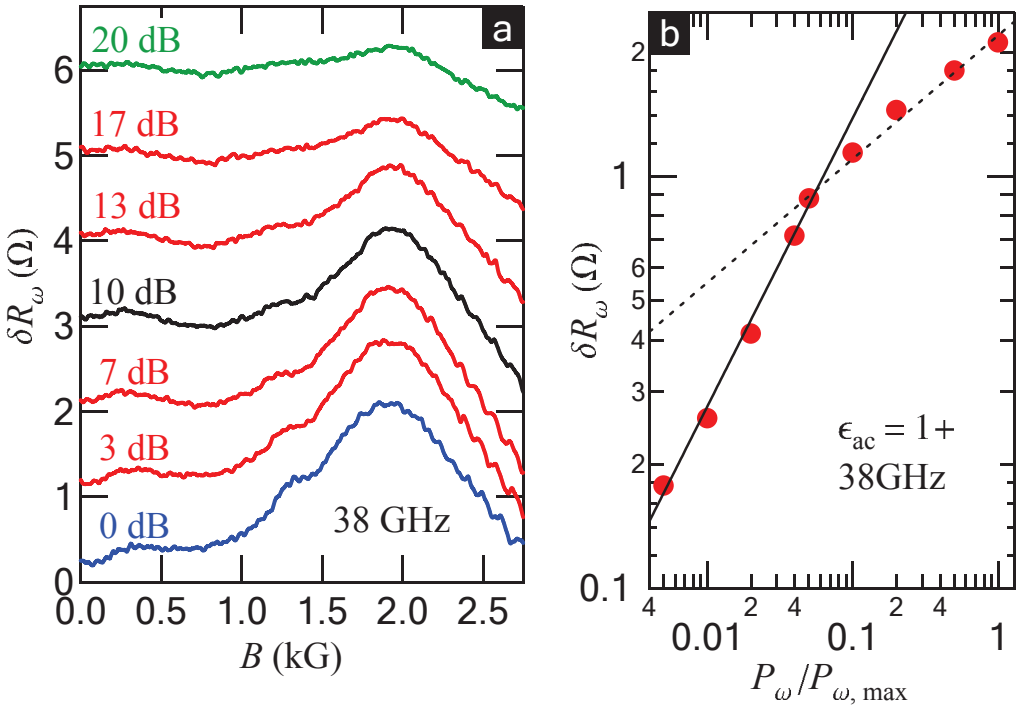

FIG. 17 (a) Microwave photoresistance with a vertical offset, δR_ω, as a function of the magnetic field, B, for various powers as indicated over 2 decades of power with $f = 38$ GHz at $T = 1.5$ K. (b) MIRO amplitude as a function of normalized applied microwave power, $\mathcal{P}_\omega/\mathcal{P}_{\omega,\,\mathrm{max}}$. The solid black line indicates $\delta R_\omega \propto \mathcal{P}_\omega^{0.7}$ behavior while the dotted line indicates $\mathcal{P}_\omega^{0.3}$ behavior.

that decreases as the power decreases. Extracting the amplitudes, we plot MIRO amplitude δR_ω as a function of normalized microwave power, $\mathcal{P}_\omega/\mathcal{P}_{\omega,\,\mathrm{max}}$, in Fig. 17 (b). At low intensities, the black solid line indicates $\delta R_\omega \propto \mathcal{P}_\omega^{0.7}$, while at higher intensities, the dotted line shows a shift in the behavior of the MIRO amplitude to increasing as $\mathcal{P}_\omega^{0.3}$. While the shift in amplitude growth rate is expected, both the growth rates in Ge are lower than expected. At low intensities, one expects $\delta R_\omega \propto \mathcal{P}_\omega$ while at high intensities one expects a shift in behavior to $\delta R_\omega \propto \mathcal{P}_\omega^{0.5}$.

C. HIRO in Ge

Recalling that HIRO requires Hall bar geometry, all the data taken in this section comes from the Ge Hall bar which has a width $w = 50$ μm with hole density $n_h = 2.66 \times 10^{11}$ cm^{-2}.

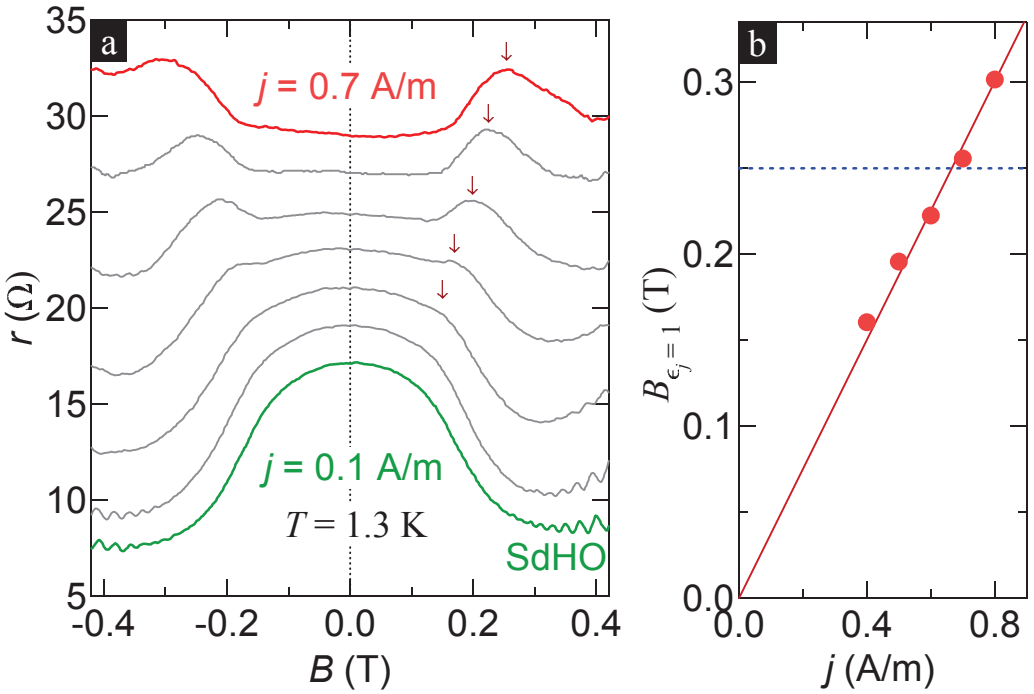

FIG. 18 (a) Differential magnetoresistance with offsets, r, plotted against magnetic field, B, for various current densities from 0.1 A/m to 0.7 A/m in steps of 0.1 A/m taken at $T \approx 1.3$ K. The first HIRO maxima is marked by arrows for the 4 highest current densities shown. The small, fast oscillations that appear on the the low current densities above $B \approx 0.3$ T are SdHO. (b) Magnetic field location of the first maxima, $B_{\epsilon_j=1}$, as a function of current density, ϵ_j. The linear fit line is used to find $m^\star = 0.11m_0$. The horizontal blue line marks $B = 0.25$ T.

We have depicted differential magnetoresistance with offsets, r, plotted against magnetic field, B, for various current densities from 0.1 A/m to 0.7 A/m in steps of 0.1 A/m in Fig. 18 (a). Peaks located symmetrically in both magnetic field directions begin from $j = 0.3$ A/m are marked with $\downarrow$ on the positive side. As expected, the peak moves to higher magnetic field and becomes larger in amplitude as current density increases.

Theoretically, Eq. (32) predicts that for any given maxima, its magnetic field location will increase linearly with current density. Thus, we have plotted the magnetic field location of the peak as a function of current density in Fig. 18 (b) and fit this data to a line. Using the slope and assuming that this is the fundamental peak ($\epsilon_j = 1$), we calculated the effective mass using Eq. (32) and found $m^\star = 0.11m_0$ which is about

20% larger than the value $m^\star = 0.088m_0$ which was obtained from MIRO earlier.

This discrepancy in $m^\star$ between MIRO and HIRO is unexpected and in order to understand what is happening here, what we first need is $\tau_{\mathrm{q},\,\omega}$ since $m^\star$ appears in both the Dingle factor and the oscillatory $\cos(2\pi\epsilon_j)$. Since there is only a single maxima, a standard Dingle analysis is impossible to do. Since we want to avoid using the condition $\omega_c\tau_{\mathrm{q},\,\omega} = 1$ which was used to estimate $\tau_{\mathrm{q},\,\omega}$ in the VdP sample which displayed MIRO, we will make use of the fact that MIRO and HIRO are supposed to have the same $\tau_{\mathrm{q},\,\omega}$; thus, we will use $\tau_{\mathrm{q},\,\omega} = 2.7$ ps, which was found from MIRO in this sample.

To look at if it is reasonable to use this $\tau_{\mathrm{q},\,\omega}$ for HIRO we directly calculate $\lambda_\omega^2\cos(2\pi\epsilon_j)$ for $j = 0.7$ A/m with $m^\star = 0.11m_0$ and plot this as a function of magnetic field, which is the blue dashed trace in Fig. 19. Doing this, one notices that while only one oscillation is visible as expected, the maxima occurs at a field much

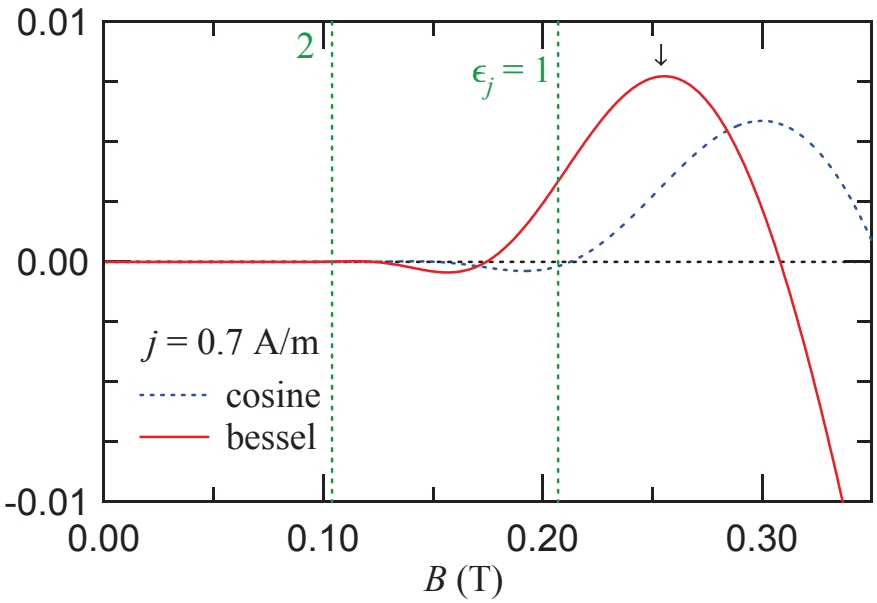

FIG. 19 The blue dashed trace is $\lambda_\omega^2\cos(2\pi\epsilon_j)$ as a function of magnetic field, B, for $j = 0.7$ A/m calculated with $\tau_{\mathrm{q},\,\omega} = 2.7$ ps and $m^\star = 0.011m_0$. The red trace is $\lambda_\omega^2 F_j(\epsilon_j)$ as a function of B for $j = 0.7$ A/m calculated with $\tau_{\mathrm{q},\,\omega} = 2.7$ ps and $m^\star = 0.088m_0$. The vertical lines indicate $\epsilon_j = 1, 2$ and both traces show just a single oscillation similar to what was seen in the measured differential resistance. The down arrow marks the first maxima, which is at $B = 0.255$ T.

higher than seen in the measured data in Fig. 18 (a). So when we ask what $\tau_{q,\omega}$ would move the peak to $B \approx 0.25$ T, we find that we would need $\tau_{q,\omega} \gg 50$ ps to get close which is very unreasonable since such a large $\tau_{q,\omega}$ should show many orders of oscillations. Since a higher $\tau_{q,\omega}$ would show more oscillations, we conclude the $\tau_{q,\omega}$ from MIRO can be used here for HIRO, and there is still an issue with $m^\star$ that needs to be resolved.

Thus, we look to another place to explain this difference in $m^\star$, namely the theory behind HIRO. Recalling that Eq. (31) was valid under the assumption that $2\pi\epsilon_j \gg 1$, which is a condition that is not well met under our current situation where $\epsilon_j \approx 1$. We can more accurately describe HIRO at lower ϵ_j by replacing the $\cos(2\pi\epsilon_j)$ in Eq. (31) with (Vavilov et al., 2007)

$$F_j(\epsilon_j) \approx \frac{\pi}{2}[J_1^2(\pi\epsilon_j) - 2\pi\epsilon_j J_0(\pi\epsilon_j)J_1(\pi\epsilon_j)] \tag{34}$$

where J_0 and J_1 are Bessel functions of the first kind. When one then plots $\lambda_\omega^2 F_j(\epsilon_j)$ as a function of B for $j = 0.7$ A/m with $m^\star = 0.11m_0$, the maxima appears at a field even higher than what is seen from $\lambda_\omega^2 \cos(2\pi\epsilon_j)$ which we plotted already. Thus, we instead plot $\lambda_\omega^2 F_j(\epsilon_j)$ as a function of B for $j = 0.7$ A/m with $m^\star = 0.088m_0$, the effective mass we got from MIRO, which can be seen as the red trace in Fig. 19. In Fig. 19, the arrow above the the red trace indicates the first maxima, which is just above $B = 0.25$ T, which is in agreement with the location of the first maxima as indicated in Fig. 13 (b). Also, we can only see one oscillation which is in agreement with what we observed in Fig. 18 (a). Thus, we can conclude that HIRO has $\tau_{q,\omega} = 2.7$ ps and $m^\star = 0.088m_0$, the same as in MIRO, and that the effective mass discrepancy stems from the condition $\epsilon_j \approx 1$ not being met, so we must use the more rigorous Bessel function representation to analyze HIRO in this case.

VI. ALLOY DISORDER

A. Introduction to Alloy Disorder

Alloy disorder scattering occurs when a 2DEG is randomly doped with a second semiconductor, making it a semiconductor solution. For example, when GaAs is

doped with Al to make a $Al_xGa_{1-x}As$ quantum well. This form of scattering is a short range scattering where the second semiconductor's atoms, which are replacing the first semiconductor's atoms, act as delta function scattering potentials. In the example given, the Al atoms would be acting as the delta function scattering potentials. This section of the thesis will report on the effects of alloy disorder scattering in $Al_xGa_{1-x}As$ quantum wells on MIRO and HIRO for samples with a low molar fraction of aluminum, x.

Since we are adding delta function scattering potentials directly into the GaAs quantum well, we expect there to be an increase in the amount of sharp scattering that occurs within the sample. We thus expect that the transport scattering time will change as the scattering within the samples change, and in fact, past studies have shown (Gardner et al., 2013) $\tau \propto x(1-x)$ which is the expected dependence (Bastard, 1988). Since both the inelastic mechanism and displacement mechanism are dependent on τ, one expects to see a response in the behavior of MIRO and HIRO in such samples.

MIRO and HIRO have garnered attention in large part for their ability to probe in depth the disorder in 2DEGs. For example, the displacement contribution is known to be very sensitive to the details in the disorder potential (Auerbach and Pai, 2007; Khodas and Vavilov, 2008), which cannot be well obtained from standard transport measurements. Also, the mixed disorder model described briefly in Sec I.B., and further expanded on later in this section, describes both the quantum lifetime and the transport lifetime in terms of the relative weights of two types of scattering events; small angle scattering off of the smooth random potential created by remote donors, $\tau_{\rm sm}$, and scattering off the random potential's short-range component, $\tau_{\rm sh}$, (e.g. from residual impurities in the quantum well).

1. Theoretical Expectations

The inelastic mechanism is also dependent on the inelastic scattering time. Under the condition that $T \gg \omega$, $\tau_{\rm in} \simeq 0.822\tau_{\rm ee}$ (Dmitriev et al., 2009), and this condition will hold true for the conditions that samples were measured under in this thesis. The

full expression for τ_{ee} is (Dmitriev et al., 2009)

$$\frac{1}{\tau_{ee}} = \frac{\pi T^2}{4E_F} \ln \frac{e^2 k_F}{\max\{\pi k_b T, \hbar\omega_c(\omega_c\tau)^{1/2}\}\, 2\bar{\epsilon}} \tag{35}$$

where $\bar{\epsilon} = 12.8\epsilon_0$ is the permittivity of the sample, and ϵ_0 is the permittivity of free space. This now gives a method of determining the contribution of the inelastic mechanism to η from Eq. (28).

To determine the contribution of the displacement mechanism, we look to the angular harmonics model described in Sec I.B. and find that (Dmitriev et al., 2009)

$$\frac{\tau}{\tau_\star} = 3\frac{\alpha z - 5z + 4}{\alpha - 4z + 3} \quad , \qquad \alpha = \frac{\tau}{\tau_{q,\,\omega}} \quad , \qquad z = \frac{\tau}{\tau_{sh}} \tag{36}$$

This leaves one needing a method to determine the sharp scattering rate found in z. In terms of angular harmonics, τ and $\tau_{q,\,\omega}$ are expressed by (Dmitriev et al., 2009)

$$\frac{1}{\tau} = \frac{1}{\tau_{sh}} + \frac{1}{\tau_{sm}}\frac{\chi}{1+\chi} \quad , \qquad \frac{1}{\tau_{q,\,\omega}} = \frac{1}{\tau_{sh}} + \frac{1}{\tau_{sm}} \tag{37}$$

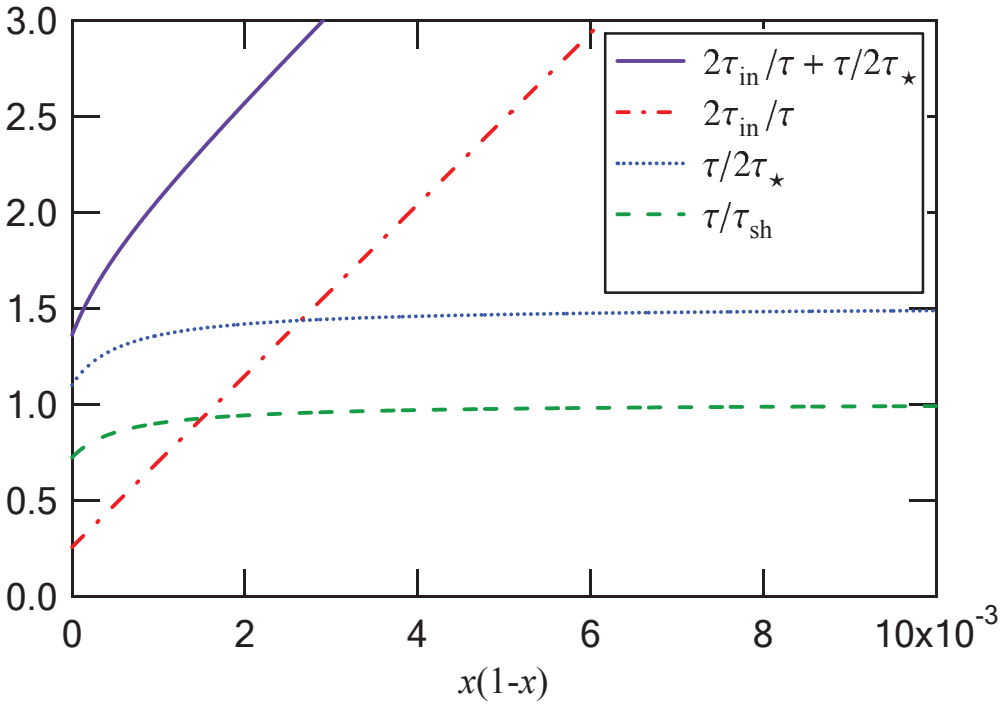

FIG. 20 Calculated dependence of displacement and inelastic mechanisms on $x(1-x)$. We used values of $T = 1.5$ K, $\tau(x=0) = 640$ ps, $\tau_{q,\,\omega} = 22$ ps, $m^\star = 0.063m_0$, and $n_e = 2.9\times10^{11}$ cm^{-2}. An alloy scattering rate of 27 ns^{-1} per %Al was applied to τ.

where $\chi = (k_F d)^{-2}$ and d is the width of the spacer. Solving this series of equations for $\tau_{\rm sh}$ yields

$$\frac{1}{\tau_{\rm sh}} = \frac{1+\chi}{\tau} - \frac{\chi}{\tau_{{\rm q},\,\omega}} \tag{38}$$

By using this angular harmonics approach, both the displacement and inelastic contributions can be calculated by extracting τ and $\tau_{{\rm q},\,\omega}$ from MIRO. Using parameters similar to those found in the samples studied, the expected behavior of both the inelastic and displacement mechanisms is calculated in Fig. 20. We see that the displacement mechanism is expected to dominate at low x, while the inelastic mechanism becomes more dominant as x increases.

Another interesting thing to note is that according to Fig. 20, if $\tau_{{\rm q},\,\omega}$ doesn't change much, then more disorder will lead to an enhancement of MIRO. However, by adding disorder, one would expect $\tau_{{\rm q},\,\omega}$ to decrease, which would lead one to believe that MIRO amplitude should decrease due to its presence in the Dingle factor, λ_ω. So there are two competing behaviors, suggesting that there may be an x where MIRO is strongest.

Alloy	x	$\rho_0(\Omega)$	$n_e(10^{11}$ cm$^{-2})$	$\mu(10^6$ cm^2/Vs)	τ(ps)	$\tau_{\rm q}$(ps)
1	0	1.31	2.93	16.3	587	19.7
3	0.00075	4.90	2.82	4.52	162	22.1
7	0.0026	9.34	2.81	2.38	85.2	17.6
9	0.0046	14.8	2.73	1.54	55.6	19.1
10	0.0078	20.2	2.54	1.21	43.5	17.4

TABLE I Table of sample parameters: sample identifier, mole fraction x, resistivity at $B = 0$ $\rho_0(\Omega)$, electron density $n_e(10^{11}{\rm cm}^{-2})$, mobility $\mu(10^6$ cm^2/Vs), and transport lifetime τ (ps) at $T \simeq 1.5$ K. Also included is quantum lifetime $\tau_{{\rm q},\,\omega}$ (ps) extracted from MIRO and shown later.

In terms of HIRO, the displacement mechanism has a dimensionless scattering time $\tau/\tau_\pi \simeq \tau/\tau_{\rm sh}$ (Khodas and Vavilov, 2008). Since we have methods to calculate both τ and $\tau_{\rm sh}$, we now have a method to analyze HIRO in terms of angular harmonics

too. As can be seen in Fig. 20, under the limit of strong short range disorder, $\tau/\tau_{\rm sh}$ approaches 1.

The alloy disorder samples reported on in this thesis are all 300 nm Hall bars that have a spacer width of $d = 75$ nm. They all underwent measurements at $T \simeq 1.5$ K, and the sample parameters can be found in Table I.

In the rest of this section we will first look at MIRO in alloy disorder, discussing quantum lifetime and transport lifetime followed by the mechanisms and amplitude. Then HIRO will be examined, focusing on the Dingle analysis and then an anomalous behavior that appears.

B. Effects on MIRO

Measured magnetoresistivity under 76 GHz microwave irradiation as a function of $\epsilon_{\rm ac}^{-1}$, which is proportional to B, is plotted in Fig. 21(a) for various amounts of alloy disorder. All of the samples show a strong response to the microwaves, producing MIRO up to at least the eighth order in each sample. By plotting magnetoresistivity against $\epsilon_{\rm ac}$, we found the effective mass for all molar fractions to be $m^\star = 0.063m_0$, which is consistent with the value of $m^\star$ obtained from other MIRO experiments and does not agree with the standard $0.067m_0$ of GaAs commonly obtained from SdHO.

1. Quantum Lifetime and Transport Lifetime in Alloy Disorder

Next, Dingle plots are constructed to obtain $\tau_{{\rm q},\,\omega}$ for each sample and they are shown in Fig. 21(b) with vertical offsets of -1 for increasing Alloy number. All of the Dingle plots are linear as one would expect and the quantum lifetimes are listed in the final column of Table I; however, the fit for Alloy 1 was done for $\epsilon_{\rm ac} > 7$ as the lower order oscillations appear irregular.

We have plotted $\tau_{{\rm q},\,\omega}^{-1}$ and τ^{-1} against $x(1-x)$ in Fig. 22(a) and fit this data to a line. τ^{-1} has a slope of 2410 ± 190 ns^{-1}, which is in agreement with past studies (Gardner et al., 2013). Since alloy disorder is not expected to contribute to $\tau_{\rm sm}$ and only to $\tau_{\rm sh}$, it is expected that τ^{-1} and $\tau_{{\rm q},\,\omega}^{-1}$ should have the same slope according

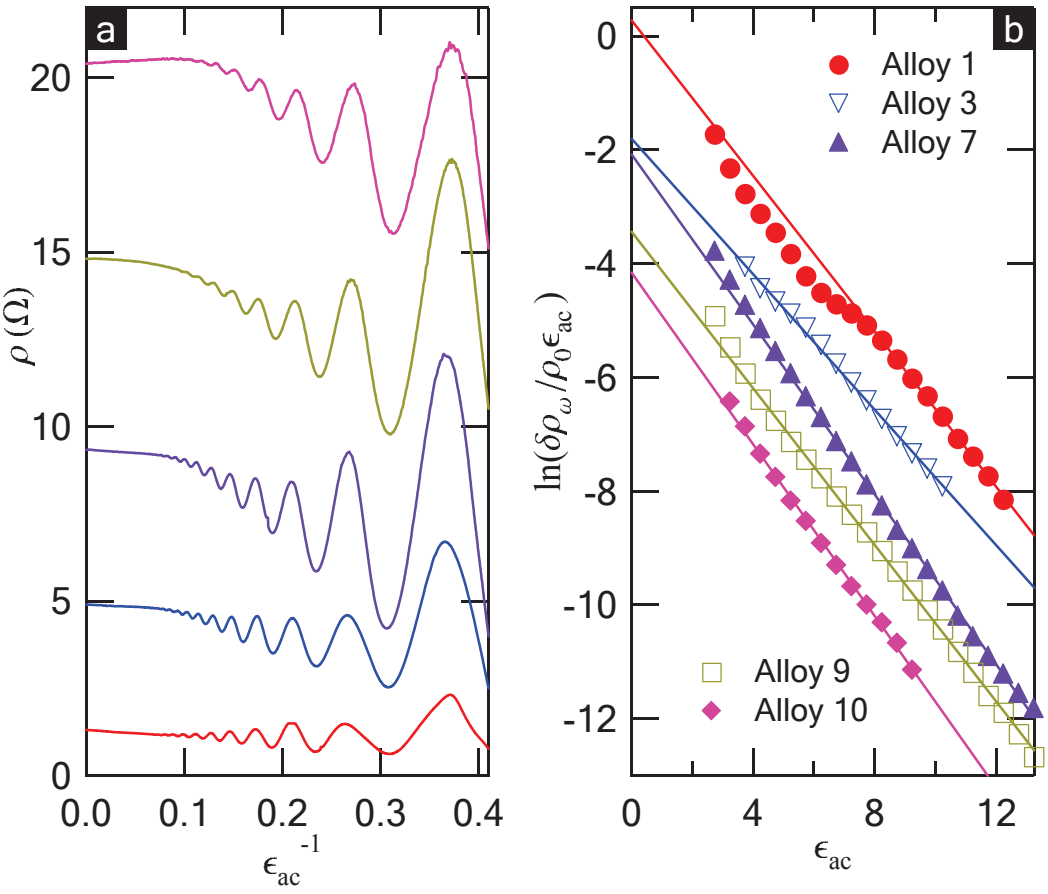

FIG. 21 (a) Measured magnetoresistivity under microwave irradiation vs $\epsilon_{\rm ac}^{-1}$. The order of samples displayed from low to high is 1, 3, 7, 9, 10. (b) Dingle plots for all samples measured with vertical offsets of -1 for increasing Alloy number. Sample numbers are listed on the plot, and the fit for Alloy 1 is done for $\epsilon_{\rm ac} > 7$.

to Eq. (37). However, $\tau_{\rm q,\,\omega}^{-1}$ has a slope of 1100 ± 660 ns^{-1}, which is greatly reduced from τ^{-1}. While this behavior agrees with what one would expect in that by adding the Al scattering centers to the quantum well, more scattering events should occur, resulting in an increased quantum scattering rate, the rate of increase of $\tau_{\rm q,\,\omega}^{-1}$ is not as large as expected. A possible contribution to this behavior is that Eq. (37) do not include temperature dependence, only the disorder potential contributions, thus alloy disorder unexpectedly appears to affect electron-electron contribution to $\tau_{\rm q,\,\omega}$.

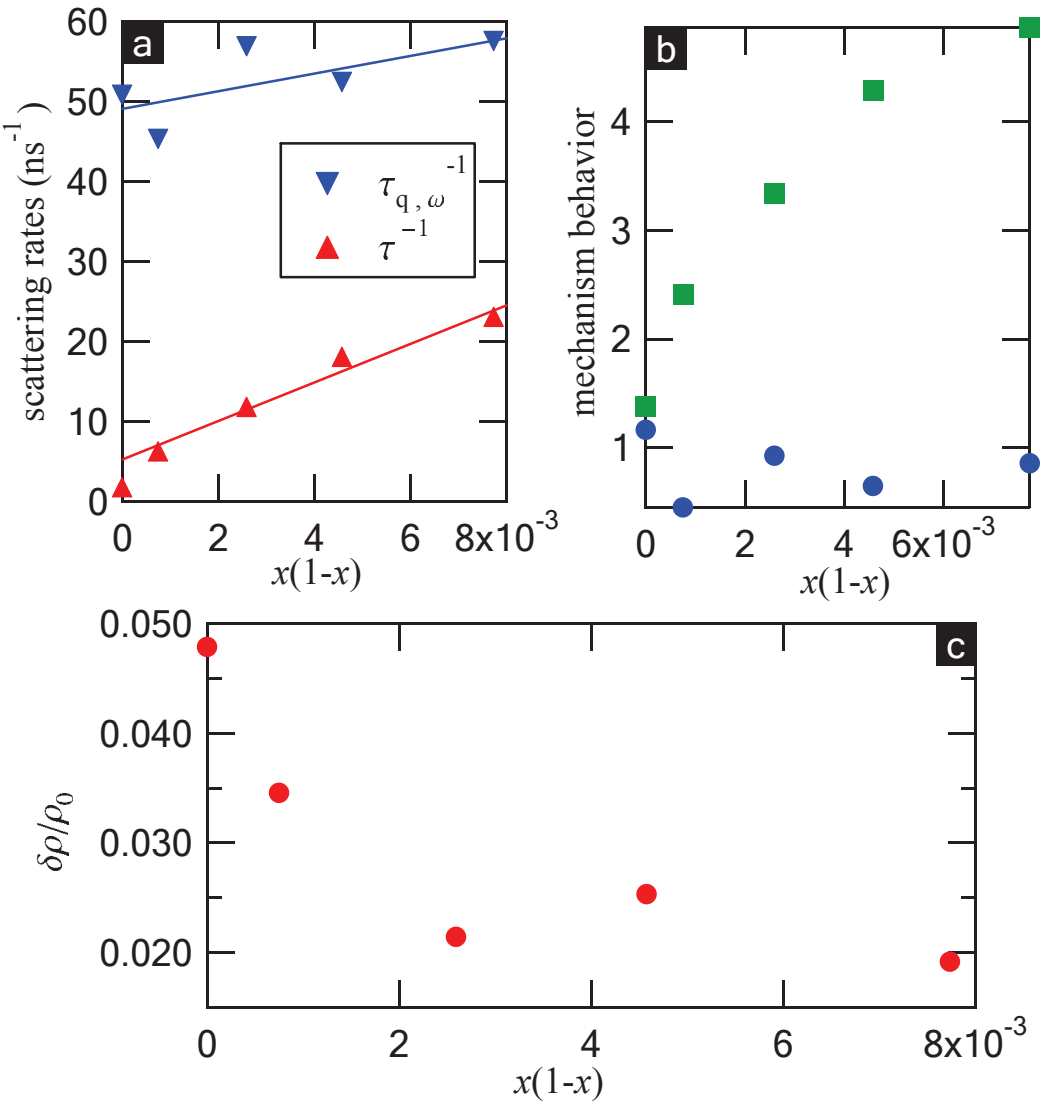

FIG. 22 (a) Quantum scattering rate ($\tau_{q,\omega}^{-1}$) and transport scattering rate (τ^{-1}) vs $x(1-x)$ and fit to a line. (b) Green squares are the sum of the contributions of the inelastic mechanism and the displacement mechanism, η, calculated using the sample parameters and the angular harmonics approach. The blue circles are $2\pi\eta\mathcal{P}_\omega$, extracted from the intercepts of the Dingle plots. (c) Normalized amplitude for $\epsilon_{ac} = 7.75$ as a function of $x(1-x)$.

2. MIRO Mechanisms and Amplitude

In order to look at the ability of the angular harmonics approach to describe the MIRO response, we have plotted the calculated dimensionless scattering rate, η, and

$2\pi\eta\mathcal{P}_\omega$, extracted from the intercepts of the Dingle plots, against $x(1-x)$ in Fig. 22(b). The calculated η were calculated with Eqs. (36),(38) using the extracted values of τ and $\tau_{\mathrm{q},\,\omega}$ listed in Table I. We cannot directly extract η from the Dingle plots because we do not have a method of completely determining the power delivered to the samples and are thus unable to separate η and $\mathcal{P}_\omega$ in our experiments. This should not matter since $\mathcal{P}_\omega$ should be a multiplicative factor that is common between each of the samples. As seen in Fig. 22, the calculated η and extracted Dingle intercepts do not have the same behavior; the extracted Dingle intercepts are unexpectedly constant.

Since the low order oscillations in Alloy 1 appear to be suppressed, we have plotted the normalized amplitude of $\epsilon_{\mathrm{ac}} = 7.75$, the lowest order oscillation that is not suppressed in Alloy 1, as a function of $x(1-x)$ in Fig. 22 (c). In Fig. 22 (c) we see the amplitude decreases with increasing alloy disorder. Since the MIRO mechanisms extracted from Dingle plots are constant and the theory predicts the mechanisms should increase with molar fraction, x, neither explain the behavior of the amplitude. Instead, the change in amplitude comes from the Dingle factor and is described by the enhancement of quantum scattering rate, $\tau_{\mathrm{q},\,\omega}^{-1}$, by alloy disorder.

C. Effects on HIRO

In Fig. 23 we have plotted measured differential resistivity with applied dc current as a function of ϵ_j^{-1} for various molar fractions. We choose to plot vs ϵ_j^{-1} instead of magnetic field due to the fact that density determines the B-field locations of the maxima and minima for HIRO. Since there are some small variations in the densities of the samples, we can see this way that all of the maxima and minima occur in the same location according to the ordering parameter. Also, we can see that Alloy 1 has no noticeable HIRO response. This is not completely unexpected because the displacement mechanism for HIRO is dependent on τ/τ_{sh}, and since Alloy 1 should have no alloy disorder, there should be very little sharp scattering occurring that could give rise to HIRO. The rest of the samples show a significant HIRO manifestation when 150 μA are applied.

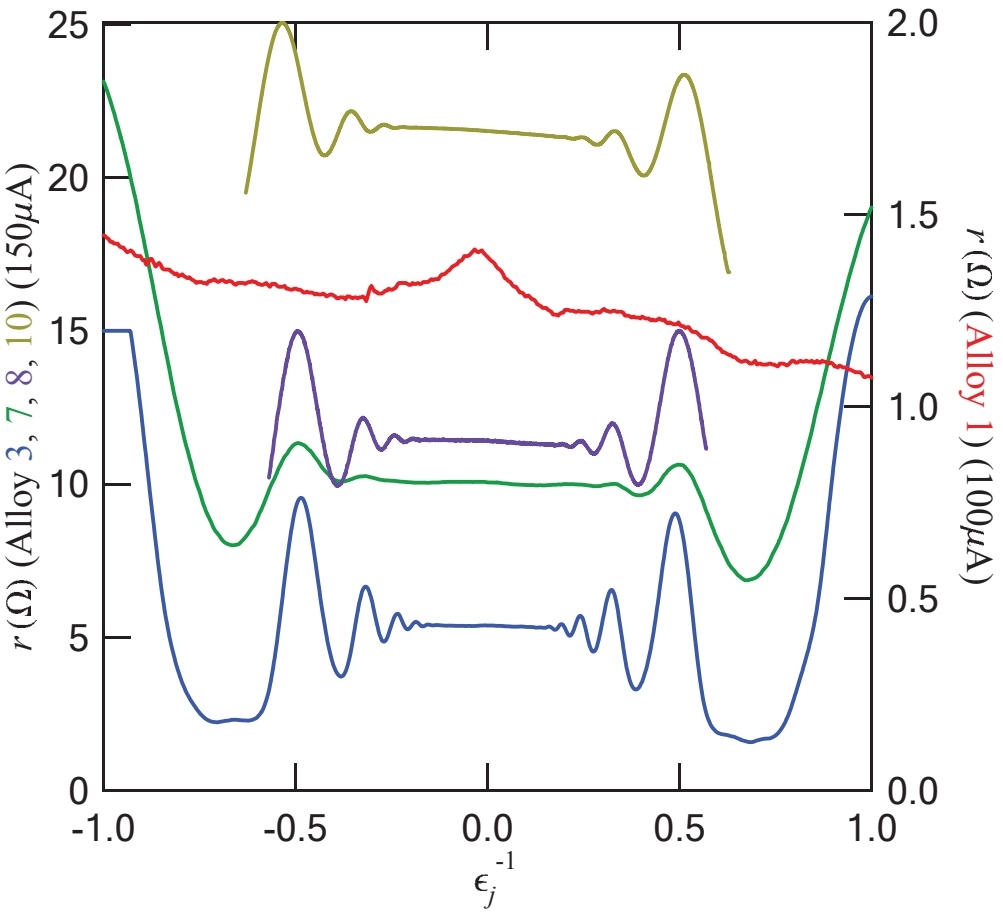

FIG. 23 Measured differential magnetoresistivity with applied dc current as a function of ϵ_j^{-1} for various samples. Alloys 3, 7, 8, and 10 use the left axis and are colored according to their listing on the left axis, and they have 150 μA of applied dc current. Also, Alloys 3, 7, 8, and 10 are the four traces showing significant HIRO response and go from low to high in the order listed. Alloy 1 is the second trace from the top and uses the right axis with 100 μA of applied dc current, and it is the trace showing no HIRO response.

1. Displacement Mechanism in HIRO

Fig. 24 (a) shows Dingle plots for the traces shown in Fig. 23, and alloys 3, 7, 8, and 10 have a similar intercept. This indicates that $\tau/\tau_{\rm sh}$ is similar for the Alloys studied under the same dc current as can be seen in Fig. 24 (b), though there are still significant differences between their values. Since we are interested in using the angular harmonics approach to describe MIRO, we can also obtain $\tau/\tau_{\rm sh}$ through calculation from Eq. (38) using the extracted τ and $\tau_{{\rm q},\,\omega}$. All of the values calculated

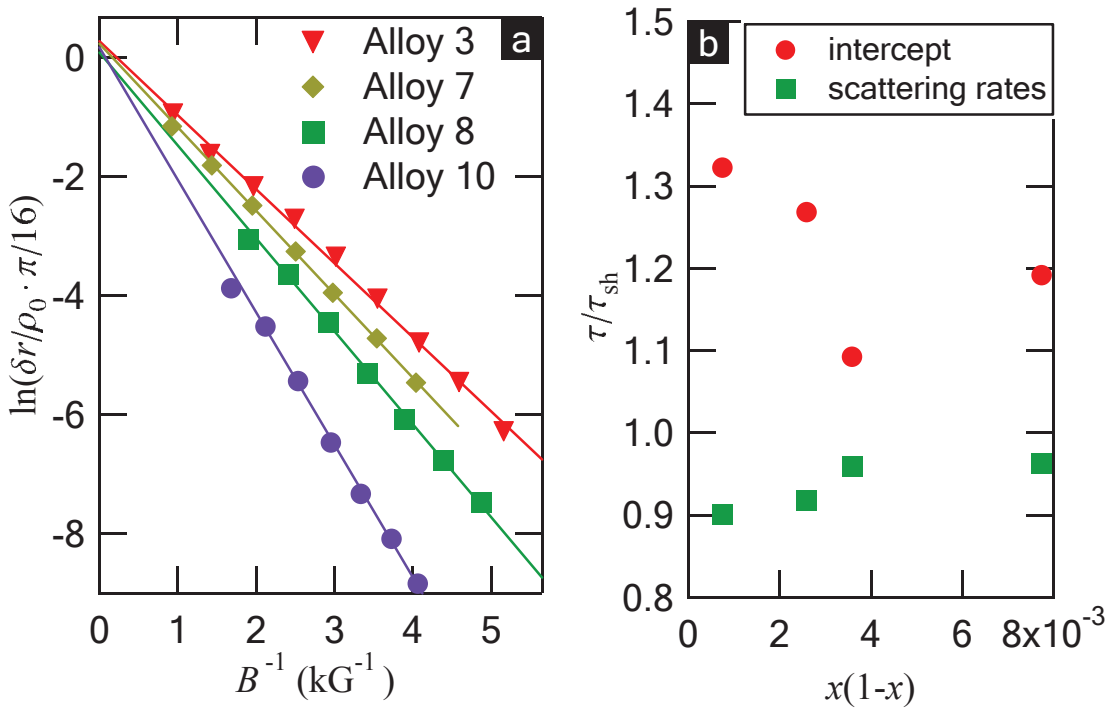

FIG. 24 (a) Dingle plots for samples studied. All samples studied share a common intercept. (b) $\tau/\tau_{\rm sh}$ plotted against $x(1-x)$ obtained from 2 different methods. The red circles were obtained from the intercepts of the Dingle plots. The green rectangles were calculated using Eq. (38).

from the scattering rates are just below 1, while the values from the Dingle plot intercepts are about 1.2. The angular harmonics approach does not reproduce the behavior of $\tau/\tau_{\rm sh}$ as obtained from HIRO data in our alloy disorder samples. Since $\tau/\tau_{\rm sh}$ should be less than 1 and the extracted values are all greater than 1 yet close to 1, we can attribute this discrepancy to uncertainty in analysis and conclude that we are not measuring this quantity accurately. Despite this discrepancy, the measured values are all near 1 and provide a good quantitative test for the theory.

2. Quantum Lifetime from HIRO

Next we take a closer look at $\tau_{\rm q,\,\omega}$ from HIRO in the alloy disorder samples. Fig. 25 shows the Dingle plots for Alloy 3 (a), Alloy 8 (b), and Alloy 7 (c). Alloys 3 and 8 each have a common intercept for the measured currents, but different slopes with the slope increasing as the current increases, thus different $\tau_{\rm q,\,\omega}$ which may be attributed

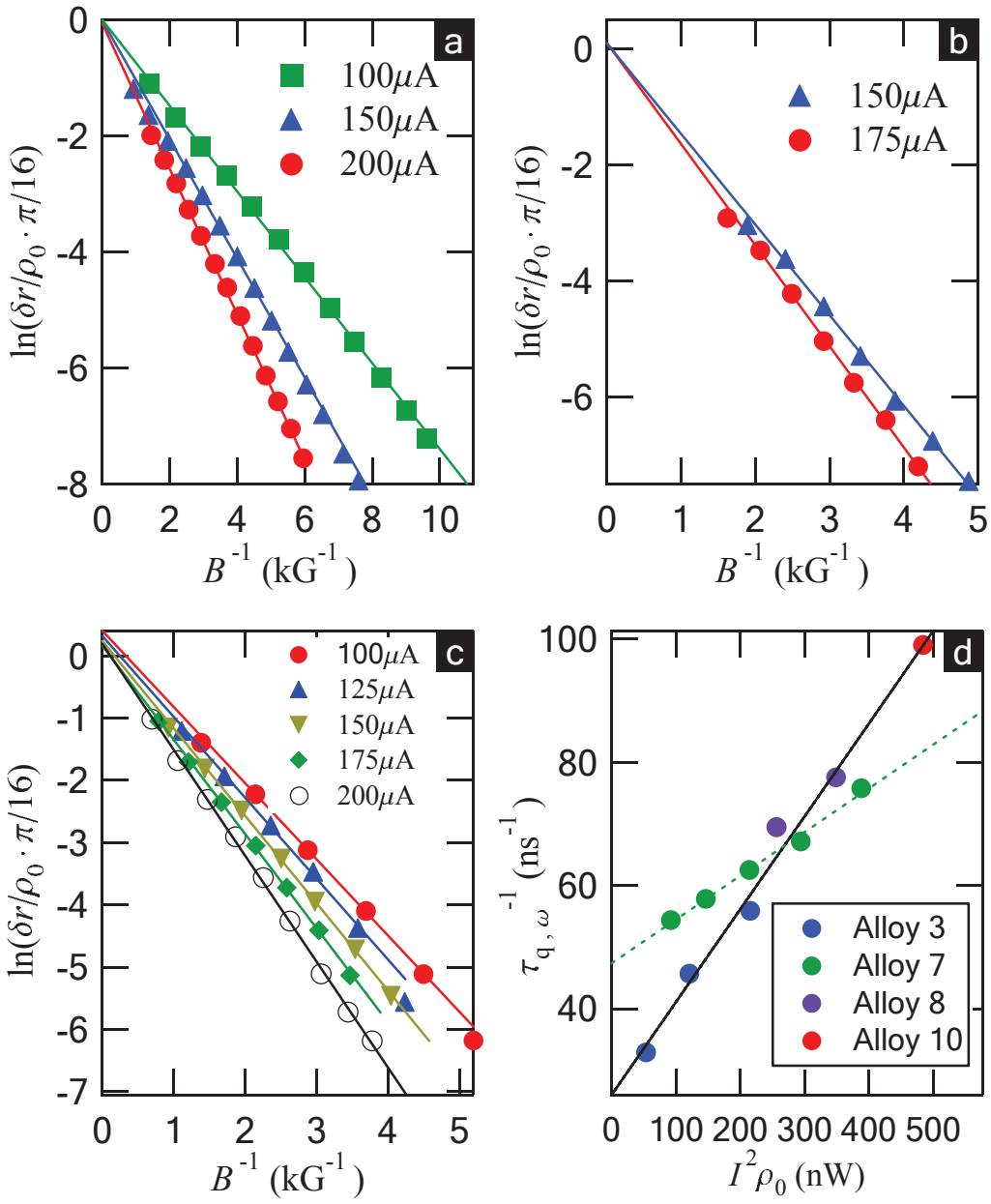

FIG. 25 Dingle plots for various currents for samples 3 (a), 8 (b), and 7 (c). (d) $\tau_{q,\omega}^{-1}$ as a function of power density in the samples with the solid black line with the larger slope fit to the points from samples 3, 8, and 10. The dashed green line with the smaller slope was fit to the points from sample 7.

to heating. Alloy 7 has slopes that follow the same trend as seen in the other samples, but the intercepts differ from each other in this sample, which is surprising since this should indicate τ/τ_{sh} is dependent on current in this sample. This unexpected behavior will be looked at more closely in the next section.

Fig. 25 (d) shows evidence that $\tau_{q,\omega}^{-1}$ may be proportional to the power density in the sample, $I^2\rho_0$. The data from Alloys 3, 8, and 10 all lie along the same line, indicated by the solid black line with the larger slope in the graph while Alloy 7's data all lie along a different line indicated by the dashed green line with the smaller slope. It is not clear whether it is expected the slope should be the same for each alloy disorder sample or if each should have its own slope in this case.

Since quantum scattering rate has such a strong response to the power density, we are unable to tell how much of the change in $\tau_{q,\omega}^{-1}$ at a given applied dc current is due to alloy disorder. Thus, we cannot compare the response of $\tau_{q,\omega}^{-1}$ to alloy disorder in HIRO to the response found in MIRO.

3. Anomalous Current Dependence

The Alloy 7 data indicated that τ/τ_{sh} may be current dependent. After a closer look, the behavior of the intercepts looks to follow the behavior of the density where the density increases as the applied DC current increases. Alloy 3 did not have a Hall measurement taken for the three currents used so this sample's density in each case is unknown, but in Alloy 8 where the intercepts were the same, the density was the same for both currents used. In Fig. 25 (c), Alloy 7 has density increase from 100 μA to 175 μA and saturates so that the densities at 175 μA and 200 μA are approximately the same, which coincides with the behavior of the intercepts of the Dingle plots where the intercept decreases from 100 μA to 175 μA and saturates so that the intercepts at 175 μA and 200 μA are approximately the same. Thus, τ/τ_{sh} decreases as density increases.

VII. EFFECTS OF DENSITY ON MIRO

A. Introduction

How MIRO depends on the carrier density has not been systematically studied and not well understood. Typically, MIRO are measured in samples of densities above $n_e \approx 2 \times 10^{11}$ cm^{-2}, and MIRO have been found to be absent in low den-

sity samples with $n_e \approx 1.6 \times 10^{11}$ cm^{-2} and $n_e \approx 0.7 \times 10^{11}$ cm^{-2} (unpublished results). Naively, the absence of MIRO in low density samples was attributed to the low sample mobility/quality. However, in a recent study, MIRO were observed in ZnO heterostructures at high densities and not at lower densities, although the higher density samples much have lower mobility and quantum lifetime due to surface roughness scatterings (Kärcher et al., 2016). This observation clearly rules out the degradation of sample quality as the main reason for absence of MIRO, and calls for further systematic studies.

According to the theory of MIRO, the variation of density could affect many aspects in deciding the MIRO amplitude. First, the variation of density could modify the interaction between electrons and the disorder potential. This affects the MIRO amplitude through both the quantum lifetime and displacement mechanism. Second, the inelastic mechanism, which is proportional to τ_{in} or the electron-electron scattering time τ_{ee} (Dmitriev et al., 2005), depends on density. Finally, the variation of carrier density also modifies the screening of the microwave radiation field. In other words, the dimensionless power (Khodas et al., 2010) deciding MIRO amplitude also varies with density.

In addition, by tuning the electron density, it is interesting to approach the regime where the second sub-band of the quantum well is filled. While the MIRO has been studied in systems with multiple sub-bands, those studies have focused on the regime when MIRO and multi-subband resistance oscillations (MISO, another class of resistance oscillations that will not be covered in this thesis) were mixing making things very complicated. Also, these studies were primarily done in double, triple, and wide quantum wells (Bykov et al., 2010, 2008; Gusev et al., 2011; Wiedmann et al., 2010a,b, 2008, 2009).

Experimentally, a systematic study on how MIRO depend on carrier density has been challenging. Studying a series of samples of different carrier density could be problematic, since the carrier density is decided by the doping scheme, and the change of carrier density would always be related to the change of disorder properties. Also, it is difficult to confirm the same experimental environment such as the microwave power if samples have to be cooled down separately.

In this study, we exploit a *in-situ* back gated sample to study the effect of density on MIRO. The sample has a 30 nm wide quantum well located 200 nm below the surface of the sample. The doped layer is in a 2 nm GaAs quantum well set on the top with a 70 nm spacer (Watson et al., 2015). The sample is a 1 mm x 1 mm VdP with $n_e = 1.63 \times 10^{11}$ cm^{-2} and $\mu = 8.9 \times 10^6$ cm^2/Vs when no gate voltage is applied. The *in-situ* gate consists of an n^+ GaAs layer located 850 nm below the bottom of the quantum well. The mobility varied from $\mu \approx 0.4 \times 10^7$ to 1.2×10^7 cm^2/Vs over the densities studied, which ranged from $n_e \approx 1.26 \times 10^{11}$ to 4.05×10^{11} cm^{-2}.

The rest of this section is organized as follows. First we briefly discuss the raw data in VII.B. Then we look more closely at how density affects effective mass (VII.B.1), the phase(VII.B.2), the quantum lifetime (VII.B.3) and the amplitude (VII.B.4) of MIRO.

B. Experimental Results

MIRO were measured under microwaves of the frequency 34 GHz at $T = 1.5$ K and 0.4 K using the standard lock-in technique described in the introduction. Photoresistance was also measured at $T = 0.4$ K using the double-modulation technique as described at the end of (Sec I. E.). In Fig. 26 we show the magnetoresistance under microwaves at $T = 0.4$ K for $n_e = 1.26$ to 3.31×10^{11} cm^{-2} in steps of 0.15×10^{11} cm^{-2} and $n_e = 4.05 \times 10^{11}$ cm^{-2}.

The top thin red trace with a zero-field resistance of about 7.8 Ω is taken at the lowest density. As the density increases, the background resistance and the amplitude of the MIROs both decrease, and then the background resistance saturates for the 3 densities just before the population of the second sub-band (traces with the lowest resistances). The second sub-band starts to get populated at $n_e = 3.31 \times 10^{11}$ cm^{-2} (lower thick black trace). As the second sub-band is populated, the background resistance increases again and MIRO become very weak. As density is further increased, both the background resistance and the MIRO amplitude increase (higher thick black trace).

We note that the oscillations occurring for $B > 1$ kG are SdHO on the thin red

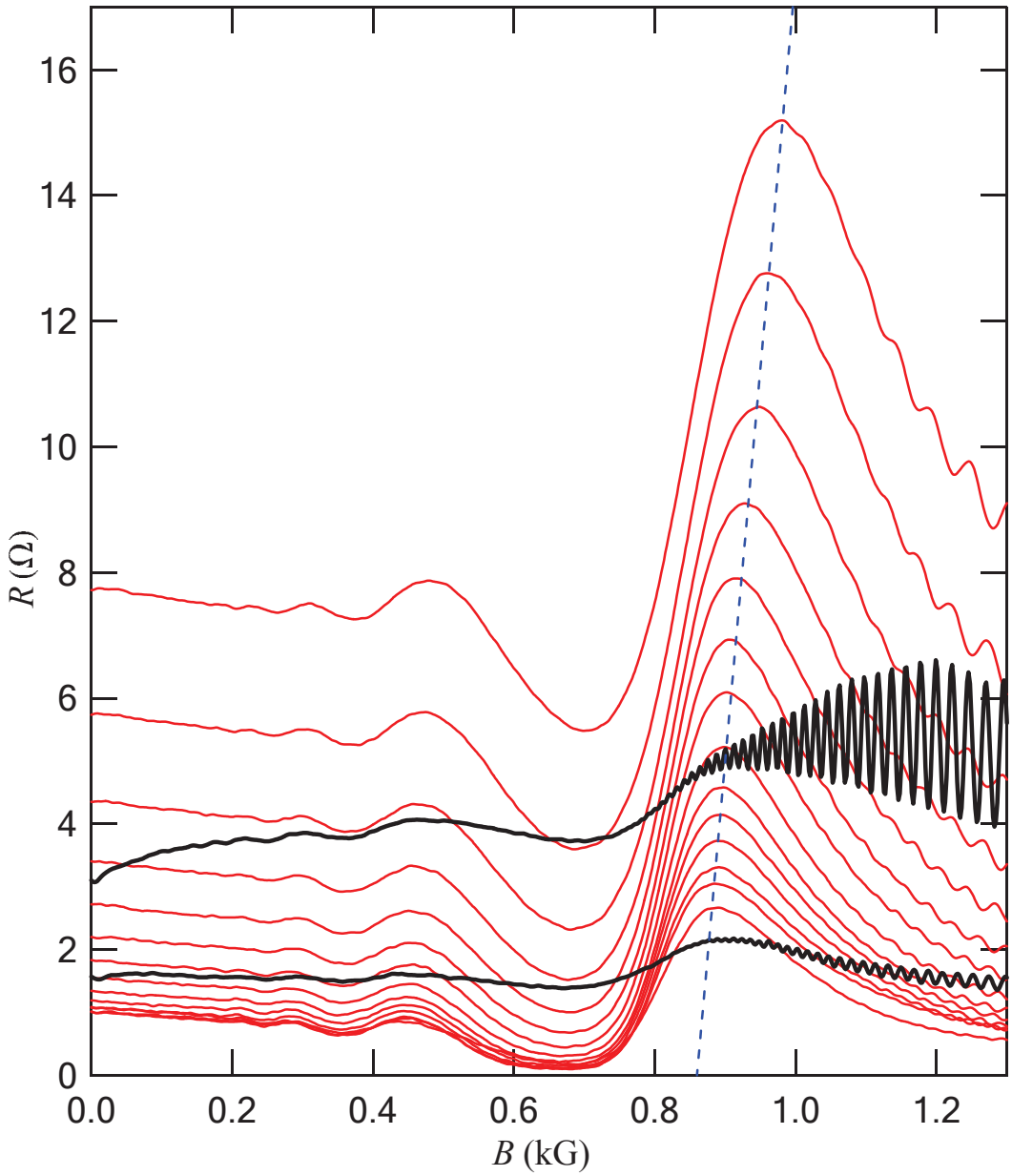

FIG. 26 Measured magnetoresistance under microwave irradiation vs. B at $T = 0.4$ K for densities from $n_e = 1.26$ to 3.31×10^{11} cm^{-2} in steps of 0.15×10^{11} cm^{-2} and $n_e = 4.05 \times 10^{11}$ cm^{-2}. The top thin red trace is the lowest density, with density increasing as the background resistance decreases. The two thick black traces with highly suppressed MIRO are the highest densities with the bottom one being the lower of the two highest densities shown, $n_e = 3.31 \times 10^{11}$ cm^{-2}. The dashed blue line follows the motion of the first maxima, indicating a change in either phase and/or $m^\star$.

traces, which have increasing frequency with increasing density. When the second sub-band becomes populated, the higher field oscillations are now a mixture of both SdHO and MISO, which will not be investigated in this thesis.

1. Density's Effect on Effective Mass

It is already noticeable from Fig. 26 that the MIRO move to lower fields with increasing density, although the radiation frequency is fixed. This is most clearly seen in the maxima of the first oscillation, where we have drawn a blue dashed line that passes through the maxima. This observation suggests that the electron effective mass decreases with increasing density.

It is well established that the effective electron mass $m^\star$ in GaAs/AlGaAs-based 2DEG can deviate from the band mass of bulk GaAs, $m_b = 0.067\, m_0$ (m_0 is the free electron mass). One cause for this deviation is the non-parabolicity of the GaAs conduction band which leads to an enhancement of $m^\star$ with respect to m_b. This enhancement becomes more pronounced at higher carrier densities and/or in narrower quantum wells. Another important aspect is electron-electron interactions which, depending on the carrier density n_e, can either increase or decrease $m^\star$ (Asgari et al., 2005; Asgari and Tanatar, 2006; Coleridge et al., 1996; Drummond and Needs, 2009; Hatke et al., 2013; Kwon et al., 1994; Smith et al., 1992; Tan et al., 2005; Zhang and Das Sarma, 2005). Since cyclotron resonance is immune to interactions (Kohn, 1961), one usually resorts to $m^\star$ measurements using Shubnikov-de Haas oscillations (SdHO) to pick up these effects (Coleridge et al., 1996; Tan et al., 2005), as discussed in II.C. However, obtaining $m^\star$ from SdHO is very time consuming as it requires magnetoresistance measurements at several different temperatures followed by a careful analysis. Furthermore, the SdHO method suffers from a relatively low accuracy even if the data reduction procedure seems to work properly (Coleridge et al., 1996; Coleridge, 1991; Hayne et al., 1992, 1997). Below we discuss study the change of $m^\star$ with density through MIRO, which turns out to be a more accurate and convenient option to investigate effective mass renormalization due to electron-electron interactions.

Fig. 27 shows an example of how we obtain the effective mass at a single carrier

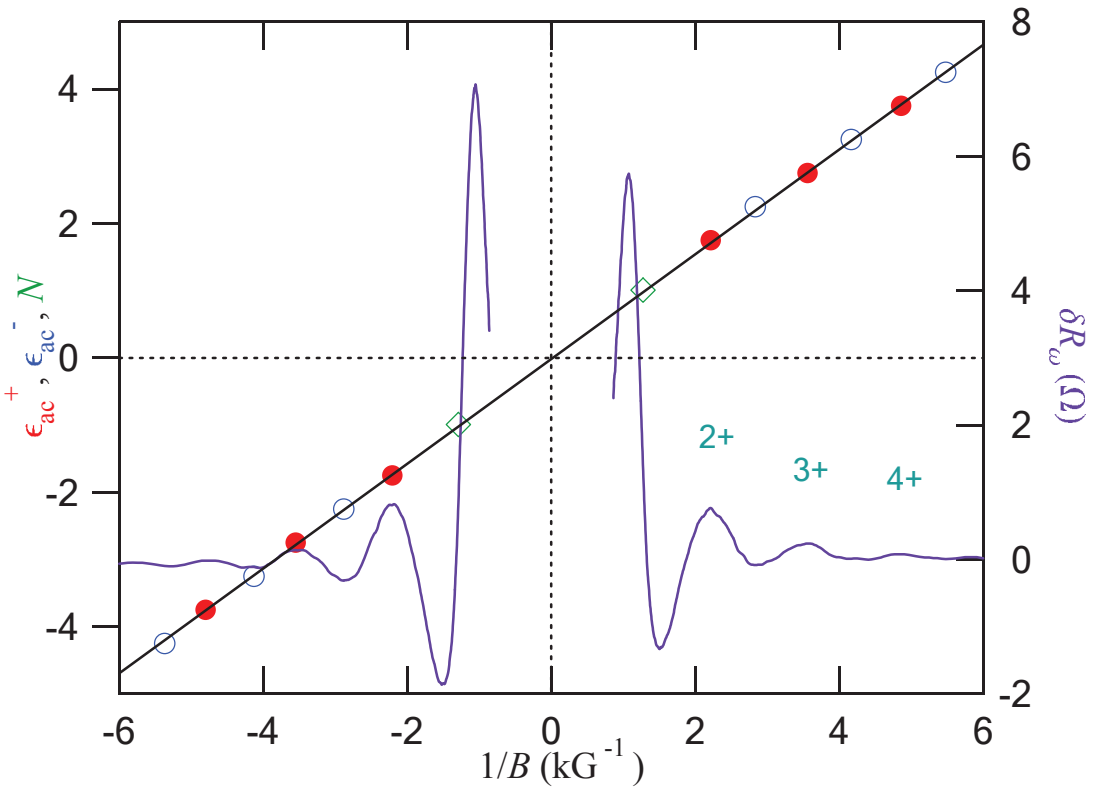

FIG. 27 Maxima ($\epsilon_{\rm ac}^{+}, \bullet$) and minima ($\epsilon_{\rm ac}^{-}, \circ$) as a function of $1/B$ for MIRO maxima and minima respectively, obtained from photoresistance δR_ω (solid line) measured at $T = 0.5$ K and $n_e = 1.64 \times 10^{11}$ cm^{-2}. Also plotted with the extrema is the node for $\epsilon_{\rm ac} = \pm 1$ ($N, \diamond$). A linear fit to the extrema and nodes gives $m^\star = 0.0652 m_0$.

density. Here, we plot the measured photoresistance for $n_e = 1.64 \times 10^{11}$ cm^{-2} as a function of B^{-1} on the right axis with maxima for oscillations 2, 3, and 4 indicated. To extract the effective mass, the maxima ($\epsilon_{\rm ac}^{+}$), the minima ($\epsilon_{\rm ac}^{-}$), and the node of the first oscillation (N) were plotted against B^{-1} and fit to a line since $\epsilon_{\rm ac} = \omega m^\star/(e_0 B)$ for MIRO. The node of the first oscillation ($\epsilon_{\rm ac} = 1$) was used because when initially plotting, the first maximum and minimum did not lie on the same line as those of the higher order oscillations. The location of the node was found by taking the average of $1/B$ for the first maximum and minimum. As can be seen in Fig. 27, all of these points lie along the same line which yields $m^\star = 0.0652 m_0$.

After repeating the effective mass extraction for other densities, we summarize our findings in Fig. 28(a) showing $m^\star$, in units of a free electron mass m_0, as a function of n_e. Here we use the high temperature, low temperature, and photoresistance measure-

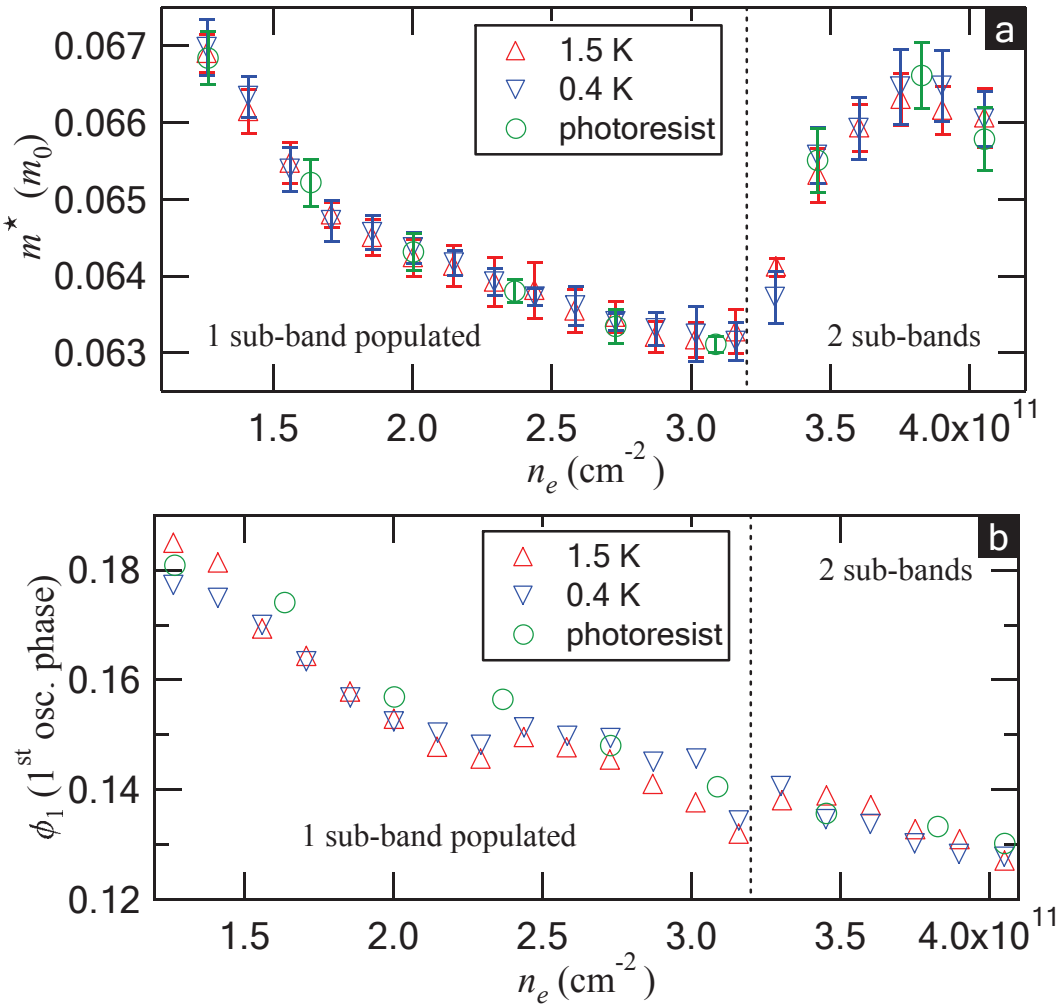

FIG. 28 (a) $m^\star$ (in units of the free electron mass) and (b) phase of the first oscillation as functions of density n_e for high temperature, low temperature, and direct measurement of photoresistance data. The vertical dashed line indicates where the second sub-band begins to be populated.

ment data, which all agree well. We first focus on the regime where only one sub-band is populated, which is plotted on the left of dashed vertical line. The effective mass starts at $0.0668m_0$ and decreases as density increases until the second sub-band begins to be populated. It is clear that at lower densities the effective mass decreases faster than at higher densities when there is only one sub-band. This behavior in one sub-band is in general agreement with another recent study on measurements of MIRO mass in a series of samples with varying densities (Shchepetilnikov et al., 2017). This is further evidence that the suppression of effective mass in MIRO is

related to electron-electron interactions as previously suggested (Hatke et al., 2013).

It is interesting to compare our findings with an earlier study which investigated the density dependence of $m^\star$ obtained from SdHO in heterojunction-insulated gate field effect transistor (HIGFET) (Tan et al., 2005). The findings of tan:2005 can be briefly summarized as follows. At low densities, between $n_e \approx 1 \times 10^{10}$ cm^{-2} and $n_e \approx 1 \times 10^{11}$ cm^{-2}, $m^\star$ showed a decrease from $m^\star \approx 0.085 - 0.1$ to $m^\star \approx 0.06 - 0.065$. However, further increase of density up to $n_e = 4 \times 10^{11}$ cm^{-2} showed either little variation of the effective mass within the experimental uncertainty (Tan et al., 2005) or a slight increase (Coleridge et al., 1996) which could have originated from non-parabolicity. This is in contrast to our data which clearly show a noticeable decrease of $m^\star$ with increasing n_e within this density range.

One possible reason for the above discrepancy is a much higher accuracy of our approach as compared to the SdHO analysis. Indeed, the uncertainty of the mass obtained in Ref. Tan et al., 2005 is comparable to the mass change detected in our experiment. However, it is also known that quantum confinement of a 2DEG under study sensitively affects mass renormalization due to electron-electron interactions (Asgari et al., 2005; Asgari and Tanatar, 2006; Zhang and Das Sarma, 2005). More specifically, the finite thickness of the 2DEG softens the Coulomb interaction potential, resulting in a reduced mass value compared to the ideal 2D case (Asgari et al., 2005; Asgari and Tanatar, 2006; Zhang and Das Sarma, 2005). Furthermore, the dependence of the quantum confinement on the gate voltage is not universal but depends on the heterostructure design. In contrast to HIGFET, the electron distribution in our quantum well becomes wider and more symmetric when a positive bias is applied to the back gate. As a result, one should exercise caution when attempting quantitative comparison of our findings with that of Ref. Tan et al., 2005 or with existing calculations (Asgari et al., 2005; Asgari and Tanatar, 2006; Zhang and Das Sarma, 2005), both of which investigated a HIGFET realization of a 2DEG.

Interestingly, when the second sub-band begins filling, a resurgence of the effective mass is seen. A complete understanding of this behavior is still missing.

2. Density's Effect on Phase

We also observe variation of the MIRO phase with density around the first cyclotron resonance harmonic. In Fig. 28(b) we plot the phase obtained from the high temperature, low temperature, and photoresistance measurement data as functions of density. For each density, the phase shown is obtained by averaging the phase for both the maxima and minima around $\epsilon_{\rm ac} = 1$ for both positive and negative magnetic fields. A continuously decreasing trend of the phase is observed, across the boundary of one and two sub-bands population, from about 0.18 to about 0.13. Again, data obtained at different temperatures agree well with each other.

The phase of MIRO is expected to decrease as the LLs become more and more separated (Dmitriev et al., 2005). However, it has not been verified by experiments; instead, one experiment has reported on essentially constant phase even when the frequency is changed in a large range, in which case one would expect the change of LL overlap. In addition, the phase of MIRO is known to decrease with increasing microwave power in the multi-photon regime at high radiation power (Hatke et al., 2011a). In our experiment, although the radiation power from the microwave source is fixed, the power experienced by the 2DEG could depend on the density due to different screening capabilities. The dimensionless power factor, $\mathcal{P}_\omega$, which characterizes the microwave field sensed by the electrons and enters the MIRO expression, is given by (Khodas et al., 2010)

$$\frac{\mathcal{P}_\omega}{\varepsilon_{\rm ac}^2} = P = \frac{e^2 v_{\rm F}^2 \tau_{\rm em}^2}{2\epsilon_{\rm eff}\hbar^2\omega^2}\left(\frac{1}{(\omega+\omega_{\rm c})^2\tau_{\rm em}^2+1} + \frac{1}{(\omega-\omega_{\rm c})^2\tau_{\rm em}^2+1}\right) \tag{39}$$

where $\varepsilon_{\rm ac}$ is the electric field of incident microwave radiation, $\tau_{\rm em} = 2\epsilon_0\sqrt{\epsilon_{\rm eff}}m^\star c/n_e e^2$, $2\sqrt{\epsilon_{\rm eff}} = \sqrt{\epsilon}+1$, and $\epsilon = 12.8$ is the dielectric constant of GaAs. In Fig. 29(a) we plot P as a function of B for two different densities. At low density, P has a more localized maximum around the cyclotron resonance; while at high density, the peak is lower and also more spread out. In Fig. 29(b) we plot P (normalized to its value at the lowest electron density at $T = 0.4$ K) at the field of the first MIRO maximum as a function of density. We observe a non-monotonic dependence of P on density, with the maximum around $n_e = 2\times10^{11}$ cm^{-2}. We thus conclude that a simple correlation between the observed phase change (Fig. 28(b) and calculated power is not feasible.

This is not too unexpected, as it is known that how the phase decreases with power could depend on the disorder properties (Hatke et al., 2011a), which also changes with density.

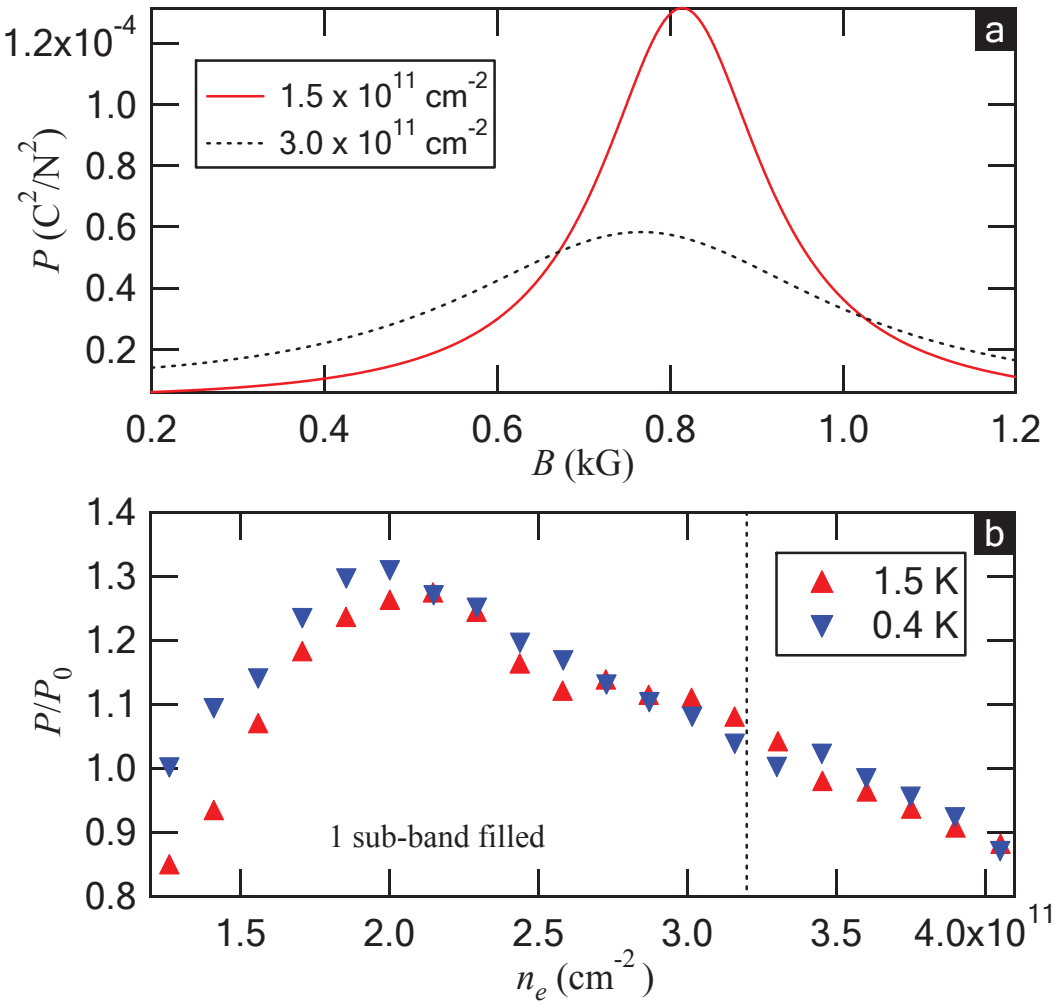

FIG. 29 (a) P as a function of magnetic field for two different densities. $n_e = 3 \times 10^{11}$ cm^{-2} uses $m^\star = 0.0632 m_0$ and $n_e = 1.5 \times 10^{11}$ cm^{-2} uses $m^\star = 0.067 m_0$, the same found in the experiments shown. (b) P normalized by P_0, the value of P at the lowest density for $T = 0.4$ K, as a function of density at the first maximum using experimental parameters. Vertical dashed line indicates the transition from 1 to 2 sub-bands.

3. Density's Effect on Quantum Lifetime

Now we examine how the quantum lifetime $\tau_{\mathrm{q},\,\omega}$ changes with density. While the quality or purity of 2DEG is usually characterized by the mobility which translates to the transport scattering time, it is known that it is only sensitive to the large angle scattering events due to sharp disorders, and is thus a poor metric for characterizing the quality of a 2DEG where small angle scattering events due to smooth disorder are abundant. In contrast, the quantum lifetime takes into account small angle scattering rates on a equal footing, and provides useful information on the disorder properties. $\tau_{\mathrm{q},\,\omega}$ is commonly measured through SdHO as discussed in II.B. However, it is well known that $\tau_{\mathrm{q},\,\omega}$ measured from SdHO could be underestimated due to small density fluctuations, since the frequency of SdHO is sensitive to density. MIRO provides a potentially more accurate option to study $\tau_{\mathrm{q},\,\omega}$ which is not sensitive to density fluctuations.

Since the power factor P (Eq. (39)) depends on density, in the Dingle analysis in this section we factor out P from the oscillation amplitudes. The Dingle plots for the first few densities, with vertical offsets of +1 for increasing density for clarity, are shown in Fig. 30(a). Also, the first minima are off the linear behavior as indicated by the points at $\epsilon_{\mathrm{ac}} = 1.25$. The points for the first maxima ($\epsilon_{\mathrm{ac}} = 0.75$) are not shown, but deviate even further than the first minima from the linear behavior of the higher order oscillations. This is expected since the phases of the first oscillation do not agree with the MIRO equation, Eq. (28).

Fig. 30 (b) shows $\tau_{\mathrm{q},\,\omega}$ vs n_e for both high and low temperature data. The vertical dotted line mark the separation between the regimes with one and two sub-bands populated. First we focus on when one sub-band is populated. In this regime, as n_e increases, $\tau_{\mathrm{q},\,\omega}$ shows a smooth increase from about 17 ps to about 24 ps. The quantum scattering rates could have contributions from both scatterings with impurities and electron-electron scatterings, $\tau_{\mathrm{q},\,\omega}^{-1} = \tau_{q,imp}^{-1} + \tau_{\mathrm{ee}}^{\text{-}1}$, where $\tau_{\mathrm{ee}}^{\text{-}1} \propto T^2/E_F$, larger at higher T and decreasing with density. Since there is no systematic difference between $\tau_{\mathrm{q},\,\omega}$ measured at the two temperatures, we conclude that $\tau_{\mathrm{q},\,\omega}$ is dominated by scattering with impurities, where the electron-electron scattering rates are much smaller, i.e,

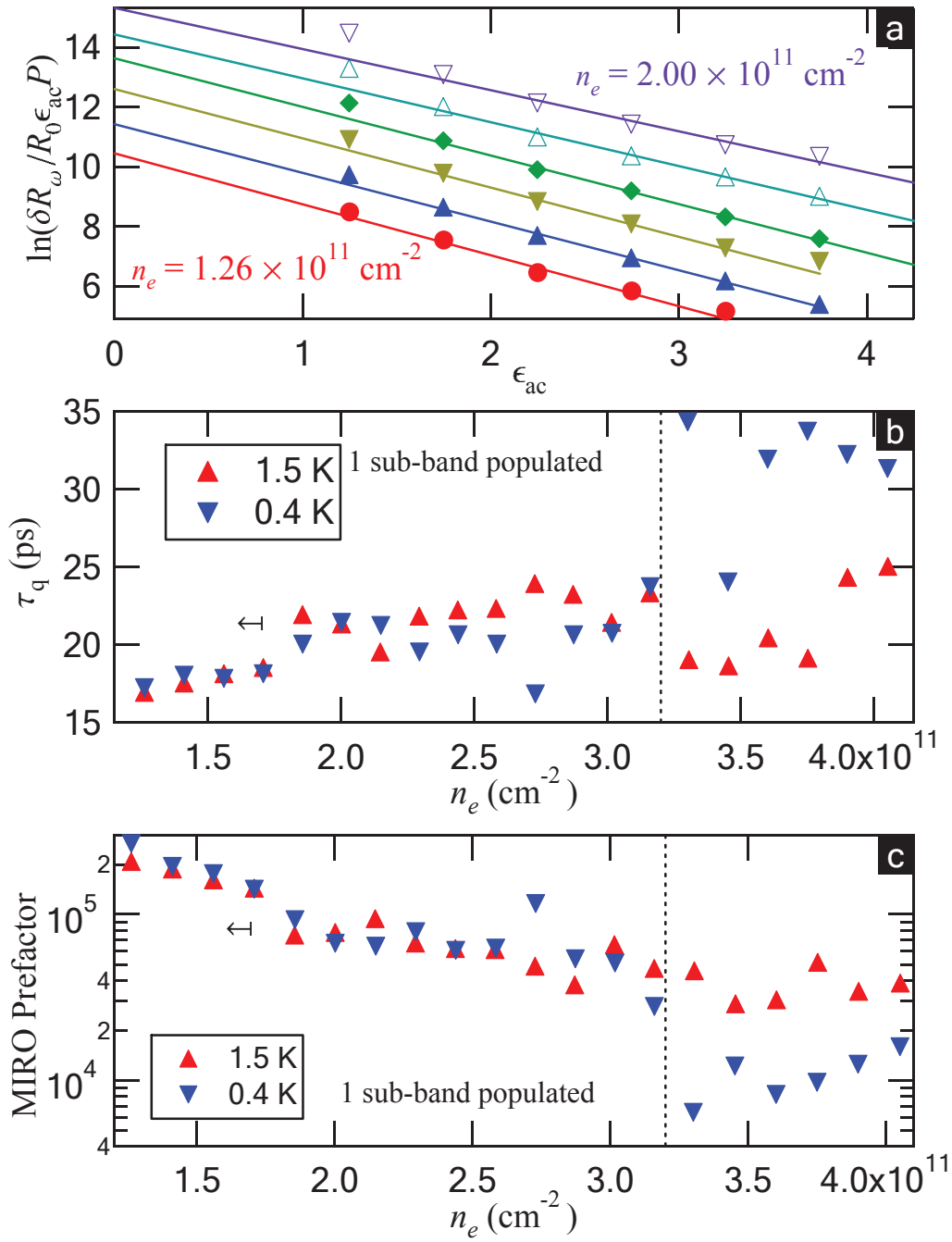

FIG. 30 (a) Dingle plots for densities from 1.26 to 2.00×10^{11} cm^{-2} in steps of 0.15×10^{11} cm^{-2} with vertical offsets +1 for increasing density for clarity. (b) $\tau_{q,\omega}$ acquired from Dingle analysis plotted against n_e. (c) MIRO prefactor, from the intercepts of the Dingle analysis, plotted against n_e with the vertical axis on a log scale. The vertical dashed line in (b) and (c) indicates the transition from one sub-band to two sub-bands. The $\mapsto$ in (b) and (c) indicate where the effective mass changes behavior with the arrow pointing to where $m^\star$ changes faster.

$\tau_{ee}^{-1} \ll \tau_{q,\omega}^{-1}$. Indeed, the lowest four densities have fairly consistent behavior, so we calculate the change in τ_{ee}^{-1} to be approximately 0.00049 ps^{-1} where as the measured $\tau_{q,\omega}^{-1}$ changes by 0.0029 ps^{-1}, a change six times larger. Thus the increase in $\tau_{q,\omega}$ with increasing density is primarily due to impurity contribution.

It is interesting to compare our results with $\tau_{q,\omega}$ measured from SdHO in a similar device (Qian et al., 2017) In (Qian et al., 2017), it was found that with increasing density, $\tau_{q,\omega}$ first increases and then finally decrease after a wide plateau before the population of the second sub-band, in contrast to the continuous increase in our measurements.

When the second sub-band becomes populated, there is clearly a dramatic increase in quantum lifetime at low temperature while at high temperature it decreases slightly. This suggests that there is something more complicated happening when there are two sub-bands populated.

Since the power was the same for each of measurement, the incident electric field, ε_{ac}, is constant, the Dingle plot intercepts (MIRO prefactor) should reflect the dimensionless scattering rates, η, up to a multiplicative factor. In Fig. 30(c) MIRO prefactor, calculated as exp(Dingle plot intercept), displayed as a function of n_e on a log-linear plot. A continuous decrease of the MIRO prefactor with density is observed. We save more detailed discussion on the amplitude MIRO in the next section.

4. Density's Effect on MIRO Amplitude

In Fig. 31(a), the amplitude of the first maximum for each of the three measurements is plotted against density. The amplitude decreases as the density increases for all data when one sub-band is filled. Once the second sub-band begins to fill, there is a sudden drop at $n_e = 3.31 \times 10^{11}$ cm^{-2} (marked by the vertical dashed line) followed by a slow increase in the amplitude.

Since the zero-field Drude resistance changes greatly with density, it plays a large role in the amplitude of MIRO, so we normalize the MIRO amplitude by the zero-field Drude resistance in Fig. 29(b). For both data sets, there are two primary features of which to be aware. First, the normalized amplitude increases until just before the

onset of the second sub-band where shortly before the second sub-band the amplitude begins to decrease. Second, once the second sub-band becomes populated, there is a very strong suppression of MIRO. Although not plotted, the amplitudes and normalized amplitudes at other ϵ_{ac} have a very similar dependence on density.

As we have briefly discussed, the variation of density could affect many aspects in deciding the MIRO amplitude. According to Eq. (28), these can be classified as the

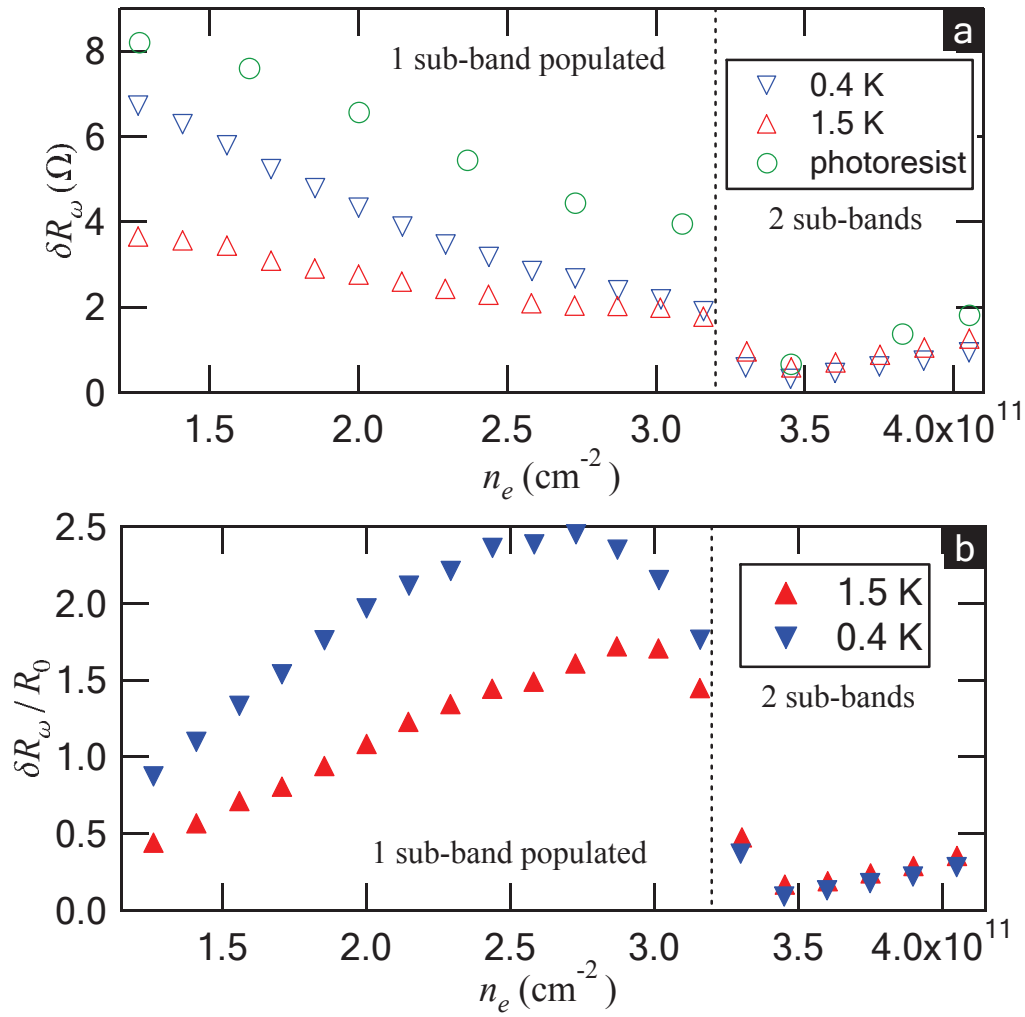

FIG. 31 (a) Amplitude of the first maximum as a function of density. All three data sets decrease until $n_e = 3.16 \times 10^{11}$ cm^{-2}, after which point the amplitudes suddenly decrease before slowly re-emerging. The temperature of the photoresistance data is $T = 0.5$ K. (b) Normalized amplitude of the first maximum as a function of density for the high and low temperature data. The transition from one energy band to two is indicated by the vertical dashed line in both graphs.

effects on (a) scattering mechanisms η (b) quantum lifetime $\tau_{\mathrm{q},\,\omega}$, and (c) the power factor P. The Dingle analysis above allows us to separate the contribution of $\tau_{\mathrm{q},\,\omega}$ from the others. Now we examine the expected change of η and P. The prefactor η contains two parts, the inelastic $2\tau_{in}/\tau$ and the displacement prefactor $\tau/2\tau_{\star}$. Since $\tau_{in} \sim n_e$ and $\tau \sim n_e^{1.5}$, the inelastic prefactor is expected to decrease with density, $2\tau_{in}/\tau \sim n_e^{-0.5}$. The displacement prefactor is also expected to decrease. On the other hand, the power factor P depends on the magnetic field or ϵ_{ac} as shown in Fig. 29(a); its density dependence is different at different ϵ_{ac}. For large ϵ_{ac}, P is larger at higher density while for the first MIRO maximum, its dependence on n_e is non-monotonic, as shown in Fig. 29(b).

Now we compare our data with the theoretical expectations. In the regime with only one sub-band population, the increase of normalized MIRO amplitude is primarily due to the increase of quantum lifetime. It is possible that the decrease of normalized MIRO amplitude for $n_e > 2.7 \times 10^{11}$ cm^{-2} while still in the one sub-band regime at low temperature is related to the power factor. On the other hand, the decrease of η with density, is consistent with the behavior of the Dingle plot intercept shown in Fig. 30(c).

The sudden drop of MIRO amplitude when the second sub-band becomes populated is puzzling. What we know about this regime is that inter-sub-band scattering rate increases sharply, which is also reflected in the increase of zero-field resistance. However, our Dingle analysis also shows that the suppression of MIRO could not be attributed to the decrease of quantum lifetime. In addition, neither η from displacement or inelastic mechanism, nor the power factor P is expected to decrease sharply. Therefore, further studies are needed to understand the effect of the second sub-band population.

VIII. CONCLUSIONS

MIRO and HIRO in Ge/SiGe 2DHG have been observed, from which we obtain the effective mass $m^{\star} = 0.088m_0$ and quantum lifetime $\tau_{\mathrm{q},\,\omega} = 3.7$ ps. The observations not only extend the study of non-equilibrium quantum transport in high LLs of

2DEGs out of GaAs, but also provide guidance for further studies in Ge 2DHG. Understanding the transport properties of this material might be important for further development of Ge-based devices which are being considered for non-silicon semiconductor technology (Pillarisetty, 2011).

We have studied the effect of alloy disorder on MIRO and HIRO. The quantum scattering rate extracted from MIRO was found to increase at a much slower rate than transport scattering rate, which is unexpected. In addition, the MIRO prefactor that is decided by scattering times, was not found to have a measurable change with increasing alloy disorder concentration. These findings challenge our current understanding of the role of disorder in MIRO, and provide guidance for further theoretical investigations.

On the other hand, we found that HIRO in the alloy disorder samples are well described by the theory, that the amplitude of HIRO is controlled by sharp disorder scattering contribution in mobility. The alloy disorder samples in our study serve as a unique series of samples with the mobility dominated by sharp disorder scattering, that is, $\tau/\tau_{\mathrm{sh}} \approx 1$. Indeed, we obtain $\tau/\tau_{\mathrm{sh}} \approx 1$ from HIRO Dingle plots of the alloy disordered samples. Our study provides a good quantitative test for HIRO theory. In addition, we have observed that the quantum lifetime $\tau_{\mathrm{q},\,\omega}$ decreases with increasing disorder. However, a quantitative comparison of $\tau_{\mathrm{q},\,\omega}$ between different samples is not feasible, since $\tau_{\mathrm{q},\,\omega}$ also decreases with increasing current, which is expected from Joule heating, and heating is different in samples of different resistance.

The effects of density on MIRO were investigated, in both regimes with one and two sub-bands population. When only one subband is populated, the effective mass decreases as the density increases, due to electron-electron interaction. Our study proves MIRO to be an accurate and convenient option to investigate effective mass renormalization due to electron-electron interactions. In addition, the phase of the first oscillation decreased as the density increased, which is opposite to what is expected. Further exploration into this is needed to fully understand the relation of phase to multi-photon processes. Furthermore, we observe a smooth increase of quantum lifetime, which contributes to an increase of MIRO amplitude (normalized by Drude resistance). After factoring out the Dingle factor, we found that the MIRO prefactor

which depends on scattering times decreases with density in the regime with only one sub-band populated, in qualitative agreement with the displacement and inelastic mechanism.

In the regimes when the second sub-band of the quantum well is also populated, there are several interesting observations which remains not understood. First, the effective mass increases sharply after the second sub-band is populated, and then saturates at a value slightly below the band mass. Second, the MIRO amplitude drops sharply after the second sub-band is populated, and then slightly increases as density is further increased. This sharp drop cannot be attributed to the drop of quantum lifetime. Further studies are needed in order to elucidate the mechanism of MIRO in this regime.

REFERENCES

Asgari, R., B. Davoudi, M. Polini, G. F. Giuliani, M. P. Tosi, and G. Vignale. "Quasiparticle self-energy and many-body effective mass enhancement in a two-dimensional electron liquid." Phys. Rev. B **71**, 045323 (2005). http://link.aps.org/doi/10.1103/PhysRevB.71.045323.

Asgari, R. and B. Tanatar. "Many-body effective mass and spin susceptibility in a quasi-two-dimensional electron liquid." Phys. Rev. B **74**, 075301 (2006). http://link.aps.org/doi/10.1103/PhysRevB.74.075301.

Auerbach, A. and G. V. Pai. "Nonlinear current of strongly irradiated quantum Hall gas." Phys. Rev. B **76**, 205318 (2007). http://dx.doi.org/10.1103/PhysRevB.76.205318.

Bastard, G. *Wave Mechanics Applied to Semiconductor Heterostructures.* Halsted Press, New York (1988).

Bykov, A. A., A. V. Goran, and S. A. Vitkalov. "Interference of magneto-intersubband and phonon-induced resistance oscillations in single GaAs quantum wells with two populated subbands." Phys. Rev. B **81**, 155322 (2010). http://dx.doi.org10.1103/PhysRevB.81.155322.

Bykov, A. A., D. R. Islamov, A. V. Goran, and A. I. Toropov. "Microwave photoresistance of a double quantum well at high filling factors." JETP Lett. **87**, 477 (2008). http://dx.doi.org/10.1134/S0021364008090063.

Bykov, A. A., J.-Q. Zhang, S. Vitkalov, A. K. Kalagin, and A. K. Bakarov. "Zero-Differential Resistance State of Two-Dimensional Electron Systems in Strong Magnetic Fields." Phys. Rev. Lett. **99**, 116801 (2007). http://dx.doi.org/10.1103/PhysRevLett.99.116801.

Coleridge, P., M. Hayne, P. Zawadzki, and A. Sachrajda. "Effective masses in high-mobility 2D electron gas structures." Surf. Sci. **361-362**, 560 (1996). http://www.sciencedirect.com/science/article/pii/0039602896004694.

Coleridge, P. T. "Small-Angle Scattering in Two-Dimensional Electron Gases." Phys. Rev. B **44**, 3793 (1991).

Coleridge, P. T., R. Stoner, and R. Fletcher. "Low-field transport coefficients in GaAs/$Ga_{1-x}Al_x$As heterostructures." Phys. Rev. B **39**, 1120 (1989). http://dx.doi.

org/10.1103/PhysRevB.39.1120.

Davies, J. H. *The Physics of Low-Dimensional Semiconductors.* Campbridge University Press (1998).

Dmitriev, I. A., M. Khodas, A. D. Mirlin, D. G. Polyakov, and M. G. Vavilov. "Mechanisms of the microwave photoconductivity in two-dimensional electron systems with mixed disorder." Phys. Rev. B **80**, 165327 (2009). http://prb.aps.org/pdf/PRB/v80/i16/e165327.

Dmitriev, I. A., A. D. Mirlin, and D. G. Polyakov. "Cyclotron-Resonance Harmonics in the ac Response of a 2D Electron Gas with Smooth Disorder." Phys. Rev. Lett. **91**, 226802 (2003). http://dx.doi.org/10.1103/PhysRevLett.91.226802.

Dmitriev, I. A., A. D. Mirlin, D. G. Polyakov, and M. A. Zudov. "Nonequilibrium phenomena in high Landau levels." Rev. Mod. Phys. **84**, 1709 (2012). http://link.aps.org/doi/10.1103/RevModPhys.84.1709.

Dmitriev, I. A., M. G. Vavilov, I. L. Aleiner, A. D. Mirlin, and D. G. Polyakov. "Theory of microwave-induced oscillations in the magnetoconductivity of a two-dimensional electron gas." Phys. Rev. B **71**, 115316 (2005). http://dx.doi.org/10.1103/PhysRevB.71.115316.

Dobbie, A., M. Myronov, R. J. H. Morris, A. H. A. Hassan, M. J. Prest, V. A. Shah, E. H. C. Parker, T. E. Whall, and D. R. Leadley. "Ultra-high hole mobility exceeding one million in a strained germanium quantum well." Applied Physics Letters **101**(17), 172108 (2012). http://scitation.aip.org/content/aip/journal/apl/101/17/10.1063/1.4763476.

Drummond, N. D. and R. J. Needs. "Quantum Monte Carlo calculation of the energy band and quasiparticle effective mass of the two-dimensional Fermi fluid." Phys. Rev. B **80**, 245104 (2009). http://link.aps.org/doi/10.1103/PhysRevB.80.245104.

Du, R. R., M. A. Zudov, C. L. Yang, Z. Q. Yuan, L. N. Pfeiffer, and K. W. West. "Oscillatory and Vanishing Resistance States in Microwave Irradiated 2D Electron Systems." Int. J. Mod. Phys. B **18**, 3465 (2004). http://dx.doi.org/10.1142/S0217979204026846.

Durst, A. C., S. Sachdev, N. Read, and S. M. Girvin. "Radiation-Induced Magnetoresistance Oscillations in a 2D Electron Gas." Phys. Rev. Lett. **91**, 086803 (2003). http://dx.doi.org/10.1103/PhysRevLett.91.086803.

Gardner, G. C., J. D. Watson, S. Mondal, N. Deng, G. A. Csthy, and M. J. Manfra. "Growth and electrical characterization of Al0.24Ga0.76As/AlxGa1xAs/Al0.24Ga0.76As modulation-doped quantum wells with extremely low x." Applied Physics Letters **102**(25), 252103 (2013). http://scitation.aip.org/content/aip/journal/apl/102/25/10.1063/1.4812357.

Giuliani, G. F. and J. J. Quinn. "Lifetime of a quasiparticle in a two-dimensional electron gas." Phys. Rev. B **26**, 4421 (1982). http://dx.doi.org/10.1103/PhysRevB.26.4421.

Gusev, G. M., S. Wiedmann, O. E. Raichev, A. K. Bakarov, and J. C. Portal. "Evidence for zero-differential resistance states in electronic bilayers." Phys. Rev. B **83**, 041306 (2011).

Hatke, A. *Ph. D. Thesis*. University of Minnesota (2011).

Hatke, A. T., H.-S. Chiang, M. A. Zudov, L. N. Pfeiffer, and K. W. West. "Zero differential resistance in two-dimensional electron systems at large filling factors." Phys. Rev. B **82**, 041304(R) (2010). http://dx.doi.org/10.1103/PhysRevB.82.041304.

Hatke, A. T., M. Khodas, M. A. Zudov, L. N. Pfeiffer, and K. W. West. "Multiphoton microwave photoresistance in a high-mobility 2D electron gas." Phys. Rev. B **84**, 241302(R) (2011a).

Hatke, A. T., M. A. Zudov, L. N. Pfeiffer, and K. W. West. "Phonon-induced resistance oscillations in 2D systems with a very high electron mobility." Phys. Rev. Lett. **102**, 086808 (2009a). http://dx.doi.org/10.1103/PhysRevLett.102.086808.

Hatke, A. T., M. A. Zudov, L. N. Pfeiffer, and K. W. West. "Role of electron-electron interactions in nonlinear transport in 2D electron systems." Phys. Rev. B **79**, 161308(R) (2009b). http://dx.doi.org/10.1103/PhysRevB.79.161308.

Hatke, A. T., M. A. Zudov, L. N. Pfeiffer, and K. W. West. "Temperature Dependence of Microwave Photoresistance in 2D Electron Systems." Phys. Rev. Lett. **102**, 066804 (2009c). http://dx.doi.org/10.1103/PhysRevLett.102.066804.

Hatke, A. T., M. A. Zudov, L. N. Pfeiffer, and K. W. West. "Resistance oscillations induced by the Hall field in tilted magnetic fields." Phys. Rev. B **83**, 081301(R) (2011b). http://dx.doi.org/10.1103/PhysRevB.83.081301.

Hatke, A. T., M. A. Zudov, J. D. Watson, M. J. Manfra, L. N. Pfeiffer, and K. W. West. "Evidence for effective mass reduction in GaAs/AlGaAs quantum wells." Phys. Rev. B

87, 161307 (2013). https://link.aps.org/doi/10.1103/PhysRevB.87.161307.

Hayne, M., A. Usher, J. J. Harris, and C. T. Foxon. "Exchange enhancement of the Landau-level separation for two-dimensional electrons in GaAs/$Ga_{1-x}Al_xAs$ heterojunctions." Phys. Rev. B **46**, 9515 (1992). http://link.aps.org/doi/10.1103/PhysRevB.46.9515.

Hayne, M., A. Usher, J. J. Harris, and C. T. Foxon. "Quantum versus semiclassical analysis of the conductivity of two-dimensional electrons in a magnetic field." Phys. Rev. B **56**, 10446 (1997). http://link.aps.org/doi/10.1103/PhysRevB.56.10446.

Kärcher, D. F., A. V. Shchepetilnikov, Y. A. Nefyodov, J. Falson, I. A. Dmitriev, Y. Kozuka, D. Maryenko, A. Tsukazaki, S. I. Dorozhkin, I. V. Kukushkin, M. Kawasaki, and J. H. Smet. "Observation of microwave induced resistance and photovoltage oscillations in MgZnO/ZnO heterostructures." Phys. Rev. B **93**, 041410 (2016). https://link.aps.org/doi/10.1103/PhysRevB.93.041410.

Khodas, M., H. S. Chiang, A. T. Hatke, M. A. Zudov, M. G. Vavilov, L. N. Pfeiffer, and K. W. West. "Nonlinear Magnetoresistance Oscillations in Intensely Irradiated Two-Dimensional Electron Systems Induced by Multiphoton Processes." Phys. Rev. Lett. **104**, 206801 (2010). http://dx.doi.org/10.1103/PhysRevLett.104.206801.

Khodas, M. and M. G. Vavilov. "Effect of microwave radiation on the nonlinear resistivity of a two-dimensional electron gas at large filling factors." Phys. Rev. B **78**, 245319 (2008). http://dx.doi.org/10.1103/PhysRevB.78.245319.

Kohn, W. "Cyclotron Resonance and de Haas-van Alphen Oscillations of an Interacting Electron Gas." Phys. Rev. **123**, 1242 (1961). http://dx.doi.org/10.1103/PhysRev.123.1242.

Kozlov, V., S. Gubarev, and I. Kukushkin. "Magnetoplasma resonance in a GaAs/AlGaAs quantum well in a strong parallel magnetic field." JETP Letters **94**, 397 (2011). http://dx.doi.org/10.1134/S0021364011170085.

Kwon, Y., D. M. Ceperley, and R. M. Martin. "Quantum Monte Carlo calculation of the Fermi-liquid parameters in the two-dimensional electron gas." Phys. Rev. B **50**, 1684 (1994). http://link.aps.org/doi/10.1103/PhysRevB.50.1684.

Lei, X. L. "Current-induced magnetoresistance oscillations in two-dimensional electron systems." Appl. Phys. Lett. **90**, 132119 (2007). http://dx.doi.org/10.1063/1.2717572.

Lei, X. L. and S. Y. Liu. "Radiation-Induced Magnetoresistance Oscillation in a Two-Dimensional Electron Gas in Faraday Geometry." Phys. Rev. Lett. **91**, 226805 (2003). http://dx.doi.org/10.1103/PhysRevLett.91.226805.

Manfra, M. "Molecular Beam Epitaxy of Ultra-High-Quality AlGaAs/GaAs Heterostructures: Enabling Physics in Low-Dimensional Electronic Systems." Annu. Rev. Condens. Matter Phys. **5**, 347 (2014).

Mani, R. G., C. Gerl, S. Schmult, W. Wegscheider, and V. Umansky. "Nonlinear growth in the amplitude of radiation-induced magnetoresistance oscillations." Phys. Rev. B **81**, 125320 (2010). http://dx.doi.org/10.1103/PhysRevB.81.125320.

Mani, R. G., V. Narayanamurti, K. von Klitzing, J. H. Smet, W. B. Johnson, and V. Umansky. "Radiation-induced zero-resistance states in GaAs/AlGaAs heterostructures: Voltage-current characteristics and intensity dependence at the resistance minima." Phys. Rev. B **70**, 155310 (2004). http://dx.doi.org/10.1103/PhysRevB.70.155310.

Pillarisetty, R. Nature (London) **479**, 324 (2011).

Qian, Q., J. R. Nakamura, S. Fallahi, G. C. Gardner, J. D. Watson, S. Luscher, J. A. Folk, G. A. Csathy, and M. J. Manfra. "Quantum Lifetime in Ultra-High Quality GaAs Quantum Wells: Relationship to 5/2 and Impact of Density Fluctuations." arXiv:1704:06213 (2017).

Ryzhii, V. I. "Photoconductivity characteristics in thin films subjected to crossed electric and magnetic fields." Sov. Phys. Solid State **11**, 2078 (1970).

Sassine, S., Y. Krupko, E. Olshanetsky, Z. Kvon, J. Portal, J. Hartmann, and J. Zhang. Solid State Commun. **142**, 631 (2007).

Shchepetilnikov, A. V., D. D. Frolov, Y. A. Nefyodov, I. V. Kukushkin, and S. Schmult. "Renormalization of the Effective Mass Deduced from the Period of Microwave-Induced Resistance Oscillations in GaAs/AlGaAs Heterostructures." Phys. Rev. B **95**, 161305 (2017).

Shi, Q., Q. A. Ebner, and M. A. Zudov. "Hall field-induced resistance oscillations in a *p*-type Ge/SiGe quantum well." Phys. Rev. B **90**, 161301 (2014). http://link.aps.org/doi/10.1103/PhysRevB.90.161301.

Shubnikov, L. and W. de Haas. Leiden Commun. **207a** (1930).

Smith, A. P., A. H. MacDonald, and G. Gumbs. "Quasiparticle effective mass and enhanced g factor for a two-dimensional electron gas at intermediate magnetic fields." Phys. Rev. B **45**, 8829 (1992). http://link.aps.org/doi/10.1103/PhysRevB.45.8829.

Studenikin, S. A., M. Potemski, P. T. Coleridge, A. S. Sachrajda, and Z. R. Wasilewski. "Microwave radiation induced magneto-oscillations in the longitudinal and transverse resistance of a two-dimensional electron gas." Solid State Commun. **129**, 341 (2004). http://dx.doi.org/10.1016/j.ssc.2003.10.00.

Tan, Y.-W., J. Zhu, H. L. Stormer, L. N. Pfeiffer, K. W. Baldwin, and K. W. West. "Measurements of the Density-Dependent Many-Body Electron Mass in Two Dimensional GaAs/AlGaAs Heterostructures." Phys. Rev. Lett. **94**, 016405 (2005). http://link.aps.org/doi/10.1103/PhysRevLett.94.016405.

Vasiliadou, E., G. Mller, D. Heitmann, D. Weiss, K. von Klitzing, H. Nickel, W. Schlapp, and R. Lsch. "Collective response in the microwave photoconductivity of Hall bar structures." Phys. Rev. B **48**, 17145 (1993). http://dx.doi.org/10.1103/PhysRevB.48.17145.

Vavilov, M. G. and I. L. Aleiner. "Magnetotransport in a two-dimensional electron gas at large filling factors." Phys. Rev. B **69**, 035303 (2004). http://dx.doi.org/10.1103/PhysRevB.69.035303.

Vavilov, M. G., I. L. Aleiner, and L. I. Glazman. "Nonlinear resistivity of a two-dimensional electron gas in a magnetic field." Phys. Rev. B **76**, 115331 (2007). http://dx.doi.org/10.1103/PhysRevB.76.115331.

Watson, J. D., G. A. Csáthy, and M. J. Manfra. "Impact of Heterostructure Design on Transport Properties in the Second Landau Level of In Situ Back-Gated Two-Dimensional Electron Gases." Phys. Rev. Applied **3**, 064004 (2015). https://link.aps.org/doi/10.1103/PhysRevApplied.3.064004.

Wiedmann, S., G. M. Gusev, O. E. Raichev, A. K. Bakarov, and J. C. Portal. "Crossover between distinct mechanisms of microwave photoresistance in bilayer systems." Phys. Rev. B **81**, 085311 (2010a). http://dx.doi.org/10.1103/PhysRevB.81.085311.

Wiedmann, S., G. M. Gusev, O. E. Raichev, A. K. Bakarov, and J. C. Portal. "Microwave Zero-Resistance States in a Bilayer Electron System." Phys. Rev. Lett. **105**, 026804 (2010b). http://dx.doi.org/10.1103/PhysRevLett.105.026804.

Wiedmann, S., G. M. Gusev, O. E. Raichev, T. E. Lamas, A. K. Bakarov, and J. C. Portal. "Interference oscillations of microwave photoresistance in double quantum wells." Phys. Rev. B **78**, 121301 (2008). http://dx.doi.org/10.1103/PhysRevB.78.121301.

Wiedmann, S., N. C. Mamani, G. M. Gusev, O. E. Raichev, A. K. Bakarov, and J. C. Portal. "Magnetoresistance oscillations in multilayer systems: Triple quantum wells." Phys. Rev. B **80**, 245306 (2009). http://dx.doi.org/10.1103/PhysRevB.80.245306.

Ye, P. D., L. W. Engel, D. C. Tsui, J. A. Simmons, J. R. Wendt, G. A. Vawter, and J. L. Reno. "Giant microwave photoresistance of two-dimensional electron gas." Appl. Phys. Lett. **79**, 2193 (2001). http://dx.doi.org/10.1063/1.1408910.

Zhang, W., M. A. Zudov, L. N. Pfeiffer, and K. W. West. "Resonant Phonon Scattering in Quantum Hall Systems Driven by dc Electric Fields." Phys. Rev. Lett. **100**, 036805 (2008). http://dx.doi.org/10.1103/PhysRevLett.100.036805.

Zhang, Y. and S. Das Sarma. "Density-dependent spin susceptibility and effective mass in interacting quasi-two-dimensional electron systems." Phys. Rev. B **72**, 075308 (2005). http://link.aps.org/doi/10.1103/PhysRevB.72.075308.

Zudov, M. A. *Ph. D. Thesis*. University of Utah (1999).

Zudov, M. A., I. V. Ponomarev, A. L. Efros, R. R. Du, J. A. Simmons, and J. L. Reno. "New Class of Magnetoresistance Oscillations: Interaction of a Two-Dimensional Electron Gas with Leaky Interface Phonons." Phys. Rev. Lett. **86**, 3614 (2001). http://dx.doi.org/10.1103/PhysRevLett.86.3614.